

Master in Instrumentation and Informatics in Physics,  
Astronomy and Space Research

SIDEBAND RATIO IN DOUBLE  
SIDEBAND AND SIDEBAND-  
SEPARATING RECEIVERS WITH A  
MICHELSON INTERFEROMETER

Michela Romanini

Supervisors: Dr. A. M. Baryshev  
Dr. R. Hesper  
Dr. F. P. Mena  
Prof. dr. W. Wild



Groningen, 25 July 2007



# TABLE OF CONTENTS

<b>ABSTRACT</b> .....	4
<b>Chapter 1. INTRODUCTION</b>	<b>5</b>
1.1 Scientific background.....	5
1.1.1 Ground-based observations.....	6
1.2 Detection requirements.....	8
1.2.1 Direct detection.....	8
1.2.2 Heterodyne detection.....	9
1.3 Sideband ratio.....	11
1.4 Thesis goal and outline.....	12
<b>Chapter 2. SUPERCONDUCTOR-BASED MIXERS</b>	<b>13</b>
2.1 Phenomenology of superconductivity.....	13
2.2 Superconductor-Insulator-Superconductor junction.....	15
2.2.1 Photon-assisted tunnelling in a SIS junction.....	18
2.2.2 SIS junction as mixing element.....	18
2.2.3 Double sideband (DSB) mixers.....	19
2.2.4 Sideband-separating (2SB) mixers.....	21
<b>Chapter 3. INSTRUMENTAL SETUP</b>	<b>25</b>
3.1 The Fourier Transform Spectrometer: general description.....	25
3.2 Instrumental setup for double sideband mixers.....	28
3.2.1 Local oscillator.....	29
3.2.2 Lock-in amplifier.....	30
3.2.3 Design of the parabolic mirrors.....	30
3.3 Instrumental setup for sideband-separating mixers.....	32

<b>Chapter 4. SIDEBAND RATIO OF DOUBLE SIDEBAND MIXERS</b>	<b>35</b>
4.1 Detection with double sideband mixers.....	35
4.1.1 Direct detection measurements.....	35
4.1.2 Heterodyne detection measurements: mixer 1.....	37
4.1.3 Heterodyne detection measurements: mixer 2.....	39
4.2 Sideband ratio calculation.....	41
4.2.1 SBR results.....	41
4.2.2 Discussion of the results.....	43
4.3 Conclusions.....	46
<b>Chapter 5. SIDEBAND RATIO OF SIDEBAND-SEPARATING MIXERS</b>	<b>47</b>
5.1 Description of the standard method.....	47
5.2 Heterodyne detection measurements.....	49
5.3 Image rejection calculations.....	50
5.4 Conclusions.....	52
<b>Appendix A: SBR error calculation.....</b>	<b>53</b>
<b>Appendix B: programs with Mathematica 5.2.....</b>	<b>55</b>
<b>References.....</b>	<b>61</b>
<b>Acknowledgements.....</b>	<b>63</b>

## ABSTRACT

---

Terahertz heterodyne receivers typically use double sideband (DSB) or sideband-separating (2SB) mixers. The precise knowledge of the receiver sideband ratio (SBR) is a fundamental requirement for the calibration of the data taken with this type of receivers. At the moment the spectroscopic techniques developed for the determination of the SBR of DSB mixers (such as Martin Puppel interferometry and Gas cell technique) and 2SB mixer (such as the technique described by Kerr) are rather complicated. Here, we present sideband ratio measurements of a DSB and a 2SB receiver in the 600-720 GHz band (ALMA Band 9) using a Michelson interferometer as input filter. The main requirement for this method is that the resolution must be high enough to allow distinguishing between the upper and lower sidebands. The advantages of this method are, first, the simplicity of the experimental setup, and, second, the possibility to identify and calibrate out standing waves in the signal and local oscillator paths. For DSB receivers, our procedure allows using exactly the same receiver configuration for both direct and heterodyne detections.

Based on our results on the DSB receiver we estimate that the direct detection can be used to predict the SBR if an accuracy of 20% is sufficient. Also for the 2SB receiver we found a satisfactory agreement between the SBR calculated from the direct detection and the SBR calculated with the method described by Kerr. Further experiments are needed to improve and better understand the results for both types of mixers.

## Chapter 1

---

# INTRODUCTION

### 1.1 Scientific background

The (sub)millimeter regions (30 GHz-1 THz) of the electromagnetic spectrum, still largely unexplored for astrophysical purposes, are the most promising ones for radio astronomy and for measurements of atmospheric molecules [1].

The cold material (10-30K) which characterizes the early stages of star and planet formation and the earliest stages in galaxy formation has its peak emission in the sub-millimeter region. The origin and evolution of galaxies are closely tied to the process in which stars eject gas and dust into the interstellar medium, while at the same time gas and dust clouds in the interstellar medium collapse gravitationally to form stars and/or planets [2]. All these processes are accompanied by absorption and emission of radiation at sub-mm wavelengths. From such absorption and emission spectra, detailed information on the dynamics, structure, and elemental and isotopic abundances of these objects can be extracted, as well as on their fundamental physical properties such as density and temperature [3].

The spectral lines emitted by a single atom are associated with changes in energies of its orbiting electrons. Spectral lines of molecules are related not only to electronic energy levels, but also to molecular motions. The large majority of the rotational and vibrational transitions of molecules have characteristic wavelengths shorter than 1 cm. The spectral lines observed in atomic and molecular absorption and emission spectra correspond to transitions occurring between different energy levels, and have an intensity which depends on the transition probability, on the population of the states, and on the relative abundance of the given chemical species. Radiative transitions between different states may occur due to spontaneous emission, collisions between atoms and molecules, and to the interaction with electromagnetic

radiation and with charged particles found in interstellar space. The measurement of the intensity of different lines of the same molecular species allows assessing the physical parameters of the emitting gas, such as velocity (Doppler shift), temperature and pressure (broadness of the line). Moreover, the comparison of lines characteristic of different molecules provides information about the local chemical composition of the gas (along the line of sight).

Contrary to that of molecules, the emission spectrum of interstellar dust is continuous (black body radiation) and varies smoothly with frequency, with a higher intensity towards shorter wavelengths (Planck's law). Since the dust temperature is in the 10-100 K range, the dust emission spectrum lies in the sub-millimeter region [4].

The sub-mm range is useful also for other purposes. The study of the cosmic background radiation at sub-mm wavelengths can be used to obtain information about the Big Bang [2]. Also the chemistry of the terrestrial atmosphere can be studied in the sub-mm range through the observation of rotational transitions of gas molecules. This is useful, for example, to obtain information about the origin and progress of the greenhouse effect and the ozone depletion [5]. Other applications of sub-millimeter and Terahertz technology are medical, healthcare and security [1].

### **1.1.1 Ground-based observations**

A problem to overcome for ground-based observations in the mm and sub-mm range lies in the fact that especially the water vapour has many strong absorption lines in the sub-mm band which, because of the pressure broadening, may completely obscure sources beyond the atmosphere. Therefore very dry conditions at high altitudes are necessary to be able to observe stellar sources from Earth.

Figure 1.1 shows the atmospheric transmission at the Chajnantor site (5000 m altitude). It is seen that the sub-mm band can be divided into several sub-bands, where the atmosphere is relatively transparent. Inside these sub-bands the observations from Earth are possible. It should be noted that, even on the best

terrestrial sites, observation of water lines is still impossible. For that a spacecraft or a high-flying aircraft or balloon is needed.

The so-called Atacama Large Millimeter Array (ALMA), located at the Chajnantor site, is the largest array of telescopes to function as an interferometer. After completion the ALMA array will consist of 50 to 66 high-precision movable radio antennas, each 12 metres in diameter, placed in a variable configuration. The receivers cover the frequency range between approximately 30 and 1000 GHz split over 10 bands fitting the atmospheric windows (fig. 1.1), with an angular resolution from 0.1 to 0.01 arcsec at the highest bands with the greatest extent of the array. Figure 1.2 shows the comparison between the angular resolution of ALMA and that of other existing or planned major astronomical facilities, such as the Very Large Array (VLA), the Hubble telescope (HST) or the Very Large Telescope (VLT).

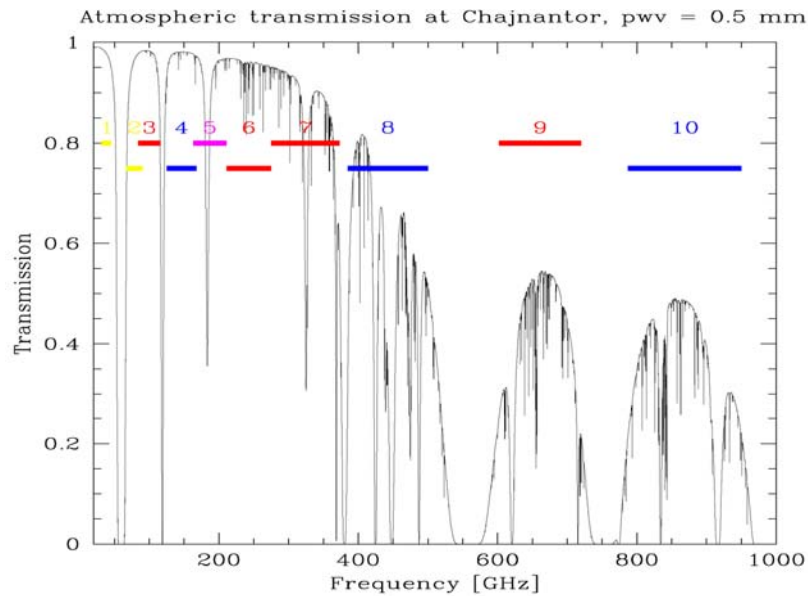


Figure 1.1: Atmospheric transmission at the Chajnantor site (5000 m altitude) together with the planned ALMA frequency bands. In winter (June-September), the precipitable water vapour column (PVW) is  $\leq 0.5$  mm for about 25% of the time (after Ref. 6).

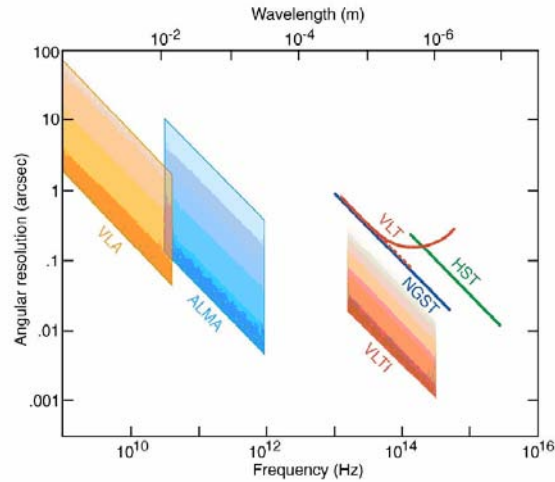


Figure 1.2: Angular resolution of ALMA compared to other major astronomical facilities (after Ref. 7).

## 1.2 Detection requirements

To obtain information on the variety and abundance of gas components present in the universe or in the Earth's atmosphere, a full spectrum over a wide wavelength range is necessary. Two basic method of detection can be used: direct detection and heterodyne detection.

### 1.2.1 Direct detection

Direct detection refers to a process in which a photon either raises the temperature of a bolometer element or causes an electron current to flow in a photoconductor. This is a power detection process in which the fundamental noise limiting the sensitivity is the signal noise. Due to limiting properties of the optics and the detector itself, the frequency band over which the sub-millimeter radiation can be observed is limited. Direct detectors are not able to resolve the phase of the detected radiation. Moreover, a direct detector can not distinguish between two signals of equal power and different radiation frequencies. Then, in order to do spectroscopy, it is necessary put a band-pass filter in front of the detector, such as a

Michelson or a Martin-Pupplett interferometer. The problem with a typical spectrometer is that the spectral resolution ( $\lambda/L$ ) is limited by the size  $L$  of the spectrometer. This is the reason why direct detection has limited applications in sub-millimeter spectroscopy when high frequency resolution and sensitivity are required. However, for broad-band mapping purposes they are excellent.

### 1.2.2 Heterodyne detection

To overcome the problems described above, heterodyne detection is used. In a heterodyne measurement, a strong local oscillator (LO) signal, of frequency close to the frequency to be detected, is combined with the weak astronomical signal from the antenna and then directed onto a non-linear detector. This detector then mixes the incoming waves and provides an intermediate frequency (IF) at the output of few GHz. The components of the down-converted signal can be separated and integrated to obtain the signal frequency spectrum.

To better explain the concept of the heterodyne mixing, let us consider a non-linear element with a current-voltage dependence given by  $I(V)=V^2$ . The incoming radiation and local oscillator signals can be represented by sinusoidal voltages:

$$\begin{aligned} V_s(t) &= V_s \sin(\omega_s t) \\ V_{LO}(t) &= V_{LO} \sin(\omega_{LO} t) \end{aligned} \quad (1.1)$$

The resulting current is given by:

$$\begin{aligned} I &= [V_s \sin(\omega_s t) + V_{LO} \sin(\omega_{LO} t)]^2 \\ &= \frac{V_s^2}{2} [1 - \cos(2\omega_s t)] + \frac{V_{LO}^2}{2} [1 - \cos(2\omega_{LO} t)] + V_{LO} V_s [\cos(\omega_s + \omega_{LO})t + \cos(\omega_s - \omega_{LO})t] \end{aligned} \quad (1.2)$$

The signal is then passed through a band filter around the IF frequency, which is defined as the difference of the LO and antenna frequencies.

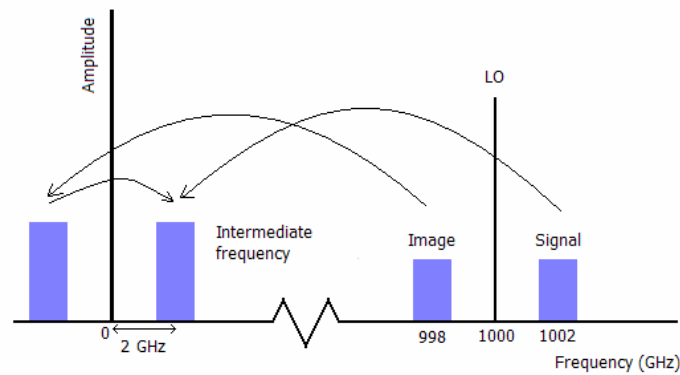


Figure 1.3: Conversion of the signal ( $\omega_{LO} + \omega_{IF}$ ) and image ( $\omega_{LO} - \omega_{IF}$ ) band during the heterodyne mixing process. The “negative” frequencies on the horizontal axis (left of the origin) are equivalent to their absolute value (right of the origin). In this example, the LO frequency is 1000 GHz, while the IF band is centred at 2 GHz.

Because negative frequencies are equal to positive ones, any down-conversion of the antenna frequency  $\omega_S$  for which  $\pm(\omega_S - \omega_{LO})$  is within the IF band passes through the filter. Hence, the IF output signal at a frequency  $\omega_{IF}$  can originate from a signal at either of the two frequencies  $\omega_S = \omega_{LO} \pm \omega_{IF}$  (fig. 1.3).

Since both the frequencies above and below the LO frequency are converted into the same IF band, the detector is said to operate in double side band (DSB) mode. The band at a frequency above the LO frequency is called upper sideband (USB) and the band at a frequency below the LO frequency is called lower sideband (LSB). Three bands of interest can be described:

- The radio frequency (RF) bandwidth, which contains the frequency of the antenna signal. The detector is sensitive to this frequency range.
- The IF band around the IF frequency (the centre frequency to which the signal is converted). The IF bandwidth determines how many spectral lines are observed at one time. The IF bandwidth is set by a band-pass filter at the IF output of the detector or limited by the detector itself.
- The LO bandwidth (or tuning range), which determines the frequencies that can actually be observed.

Figure 1.4 shows a block diagram of a heterodyne receiving system. The antenna signal is coupled with the LO signal and the spectral components of the combined beam are down-converted in the mixer. The IF signal is amplified and then analyzed by the back-end spectrometer or by a correlator. Heterodyne mixing requires a non-linear element such as a Schottky-barrier diode, a Superconductor-Insulator-Superconductor (SIS) junction or a Hot Electron Bolometer (HEB). ALMA Band 9 works with SIS junction as a mixer. Detailed information about this kind of junction is presented in section 2.2.

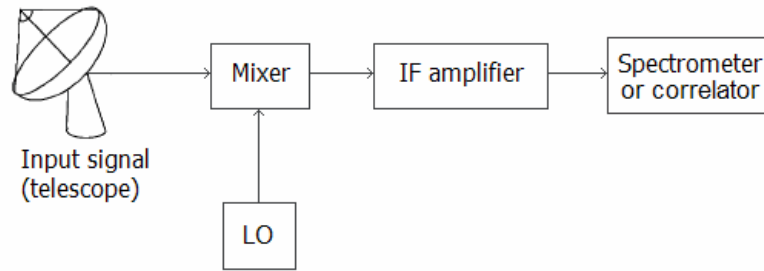


Figure 1.4: block diagram of heterodyne receiving system.

### 1.3 Sideband ratio

The output current of the mixer at a frequency  $\omega_{IF}$  contains two contributions, arising from the frequency components of the reference signal intensity at  $\omega_{LO} + \omega_{IF}$  and  $\omega_{LO} - \omega_{IF}$ , as for both these frequencies the absolute frequency difference with respect to the fixed LO frequency is within the IF band (see fig. 1.3).

Hence, the accurate calibration of a heterodyne receiver requires knowledge of the sideband ratio (SBR), which is the gain ratio between the upper and lower sideband frequencies. For an ideal double-sideband receiver the SBR is equal to one, but in practice the receiver response in the upper sideband may be different from that in the lower sideband. Therefore it is very important to know the SBR at different LO frequencies to be able to recover, from a measured spectrum, the correct relative

intensity of the various spectral lines. This is because even if a spectral line is observed in one sideband, atmospheric noise from the other sideband is superimposed on the spectrum.

At the moment the spectroscopic techniques developed for sub-millimeter analysis to determine the SBR (such as Martin Puppel interferometry [8] and Gas cell technique [9]) rely on a calibrated filter system and are rather complicated.

## **1.4 Thesis goal and outline**

In this thesis sideband ratio measurements of a sub-millimeter receiver in the 600-720 GHz band (ALMA Band 9) using a Michelson interferometer as input filter are presented. The main goal is the investigation of the relation between the direct and heterodyne mode to determine if the simple direct detection method is a reliable predictor of the SBR of double sideband mixers.

Chapter 2 contains an overview of the theory of superconductivity and the description of the type of superconducting mixers used in this thesis.

In chapter 3 the Michelson interferometer and the complete instrumental setup are described in detail.

The standard technique used to calculate the SBR for sideband-separating mixers is rather complicated [10]. Here we propose a new method to determine the SBR of sideband-separating mixers using heterodyne spectra measured with a Michelson interferometer. The experimental setup is similar to the one used during the measurements with double sideband mixers and it is also described in detail in chapter 3.

The results obtained with double sideband mixers are reported in chapter 4, and those with sideband-separating mixers in chapter 5.

# SUPERCONDUCTOR-BASED MIXERS

## 2.1 Phenomenology of superconductivity

Superconductivity was discovered in 1911 by Heike Kamerlingh Onnes and coworkers as they were conducting experiments on the resistance of metallic samples at cryogenic temperatures. The superconducting phase of a material is characterized by the absence of electrical resistivity below a critical temperature  $T_c$  (fig. 2.1) [11]. This phase also behaves as a perfect diamagnet: an external magnetic field, below a certain strength, is not able to penetrate inside the superconductor. Moreover, if a magnetic field is present at the moment that  $T$  goes below  $T_c$ , the field is expelled from the superconductor. This is known as the Meissner effect and is represented in figure 2.2. On the contrary, above  $T_c$  most superconducting materials behave as normal conductors: they display a non-zero resistivity, and an applied magnetic field penetrates uniformly through the material generating a paramagnetic response.

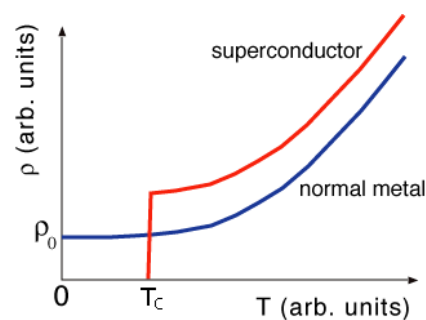


*Figure 2.1: Behaviour of the resistivity  $\rho$  as a function of temperature  $T$  for a normal metal (blue line) and a superconductor (red line).*

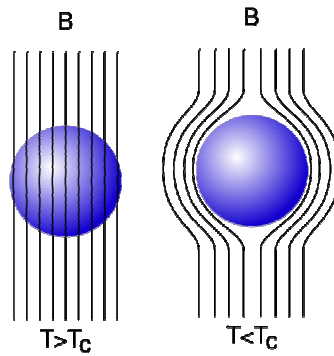


Figure 2.2: Magnetic field distribution in the normal state ( $T > T_c$ ) and in the superconducting state ( $T < T_c$ ) of a superconductor in the presence of a homogeneous external magnetic field.

Bardeen, Cooper and Schrieffer developed in 1957 the theory of conventional superconductors (known as BCS theory [12]). Electrons in solids usually repel one another due to the mutual Coulomb interaction. However, in the presence of other interactions, the net coupling between two electrons in a metal can be attractive. As an electron moves in a metallic crystal, it attracts the positive lattice ions, generating a lattice distortion (in quantum mechanical terms, it emits a phonon). This lattice distortion creates an excess local positive charge which persists also after the passing of the electron (as the speed of atomic ions is much lower than that of electrons), and is thus able to attract a second electron (which, in quantum terms, absorbs the emitted phonon).

This results in a “retarded” attractive potential mediated by the electron-phonon interaction. Although this effective attraction is weak, it is nonetheless effective as the electrons avoid meeting directly and thus do not feel their full mutual Coulomb repulsion. The attractive potential leads to the formation of electron pairs with opposite momenta and opposite spin (called “Cooper pairs”), which behave as bosons and are thus able to collapse in a Bose-Einstein-like condensate at low temperature. The BCS theory describes superconductivity as the formation of a macroscopic, coherent condensate of Cooper pairs. Since the electrons are bonded in Cooper pairs, a finite amount of energy ( $\Delta$ ) is needed to break them in two

independent electrons. Thus an energy gap  $2\Delta$  in the density of states is present (fig. 2.3) which is usually of the order of a few meV and which decreases with increasing temperature and vanishes at the critical temperature, when superconductivity ceases and the normal metallic state sets in. The presence of this gap also accounts for the lack of resistivity. The resistivity is zero because Cooper pairs have no available states close in energy to scatter into, contrary to the case of a normal metal where electron states arbitrarily close to the Fermi level are available.

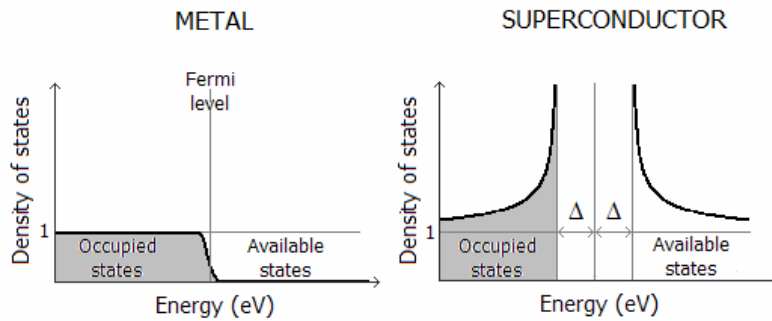


Figure 2.3: Electron densities of states for a metal at  $T>0$  (left), and a BCS superconductor at  $T=0$  (right).

## 2.2 Superconductor-Insulator-Superconductor Junction

A sequence of superconductor-insulator-superconductor layers forms a so-called SIS junction. For a thick insulating layer no current can flow between the superconductor electrodes, even if the applied potential across the junction is not zero. But if the insulator is very thin (few nanometers), a current can start to flow because of the quantum mechanical tunnelling effect. At high temperatures where the superconducting material is in the normal state, single electrons tunnel through the barrier. In the superconducting state, in the absence of pair-breaking excitations, only Cooper pairs can tunnel through the junction. The flow of Cooper pairs through a barrier or inside the superconductor is called “supercurrent”.

Figure 2.4 shows the band diagram of a SIS device when it is cooled below the critical temperature of the two superconductors.

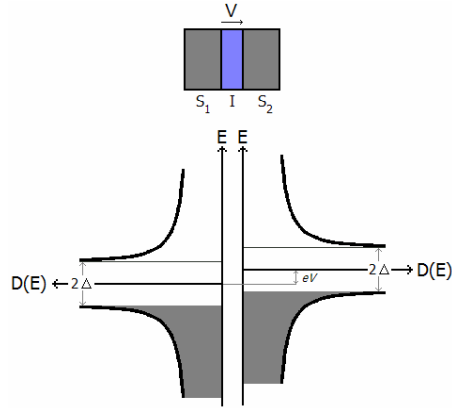


Figure 2.4: Geometry and energy band diagram of a SIS junction. The energy gap  $2\Delta$  forms when the junction is cooled below the critical temperature.

If there is no voltage difference across the barrier, the occupied states of both superconductors are aligned and only Cooper pairs from either side of the barrier can tunnel through it. This effect, known as DC Josephson effect, produces a current without generating a potential across the barrier; if the two superconductors are connected electrically at each end of the junction, such supercurrent persists forever. The maximum possible supercurrent (called the critical current of the junction  $I_C$ ) is limited by the tunnelling probability and by the density of the Cooper pairs present in the junction. With a fixed voltage across the junction, the phase will vary linearly with time and the supercurrent will be an alternate (AC) current. This is known as AC Josephson effect.

Both types of Josephson effects are related to the existence of a difference in the phase of the wavefunction of the Cooper-pair condensate across the junction. The tunnelling supercurrent can be suppressed by the application of a magnetic field across the barrier, which alters the phase difference between the condensate wavefunction at the different ends of the junction. In this way, a carefully chosen magnetic field quenches supercurrent and the only current that is flowing through the junction is due to “quasiparticles”<sup>1</sup> (“leakage current”), which are unpaired

<sup>1</sup> The ground state of the system is the condensate of Cooper pairs. In general, quasiparticles are defined as elementary excitations of a system which have particle-like properties (*i.e.*, a defined momentum, energy, mass, charge, etc.).

electrons, or to tunnelling of Cooper pairs into separate quasiparticle states. The latter process can only happen if there is enough potential energy available to break the Cooper pair (i.e.  $2\Delta$ ).

A SIS junction in which the supercurrent is suppressed exhibits a non-linear current-voltage (I-V) behaviour as shown in figure 2.5. The main features of the I-V curve of a SIS junction are:

- At voltages  $|V| < V_G$  (where  $V_G$  is the gap voltage, given by  $2\Delta/e$ ) the occupied electronic states in the two superconductors overlap in energy and there is no significant quasiparticle tunnelling through the barrier, if no other sources of excitation are available (see section 2.2.1).
- At a bias voltage  $|V| = 2\Delta/e$  the occupied states of one superconductor are aligned with the empty states in the other superconductor and Cooper pairs of the former can tunnel into quasiparticle states in the latter. The density of states diverges at the edges of the superconducting energy gaps, which causes a step-function increase in the intensity of the bias current.
- Increasing the bias voltage above the gap voltage, the SIS junction exhibits a metallic-like behaviour with a linear increase of the current with the voltage.

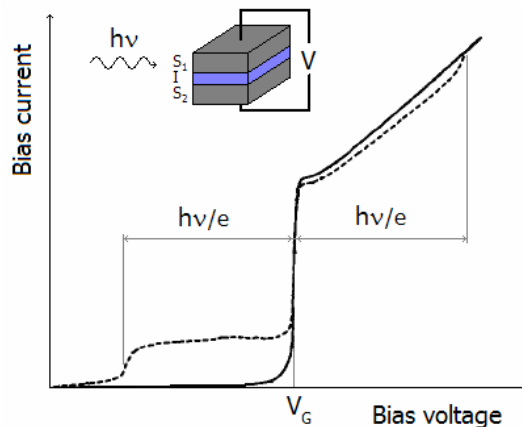


Figure 2.5: Current-voltage curve of SIS junction. The dashed line is the current-voltage curve when the SIS junction is pumped with a radiation in the sub-mm range.

### **2.2.1 Photon-assisted tunnelling in a SIS junction**

If a radiation of frequency  $\nu$  is applied across the SIS junction (that is, the SIS junction is *pumped*), photons can be absorbed by quasi-particles or by Cooper pairs. If one photon at a time is absorbed, the energy of the quasi-particles raises by the energy of a quantum  $h\nu$  (or  $nh\nu$  if  $n$  photons are absorbed at a time). If the bias voltage is in the range  $(2\Delta - nh\nu)/e < |V| < 2\Delta/e$ , then the quasiparticles or Cooper pairs can tunnel, upon light absorption, to the allowed empty states across the junction (figure 2.4). This process is named photon-assisted tunnelling and it gives rise to sharp steps in the current at voltage intervals of  $h\nu/e$ . The dashed line in figure 2.5 shows the current-voltage characteristics of a SIS junction pumped with a sub-millimeter wavelength radiation. The number of electrons tunnelling through the barrier is related to the number of photons absorbed and thus to the power of the radiation source.

### **2.2.2 SIS junction as mixing element**

A common feature of mixer components is their non-linear I-V curve in a certain range of voltages. As shown in the introduction, this non-linearity is responsible for the frequency mixing (creation of frequency combinations as the sum or difference of incoming frequencies) when two signals with different frequencies are applied. The frequency component with the difference of these two frequencies (IF) is the crucial one for heterodyne mixing. As visible in figure 2.5, SIS junctions show a non-linear I-V behaviour for bias voltage below the gap voltage. The possibility to use a SIS junction as a mixer is a consequence of this non-linearity and of the quantum-mechanical nature of the photon-assisted tunnelling [13]. When a time-varying voltage  $V(t)$  is applied to a SIS junction of which one side is connected to ground, the quasiparticle energy eigenstates on the ungrounded side of the barrier are modulated by a phase factor  $f(t)$ . From this factor, the current that tunnels through the device can be written as:

$$i(t) = \frac{1}{2} \sum_{n=-\infty}^{\infty} I(n) e^{jn\omega t} \quad (2.1)$$

where  $I(n)$  are complex currents (current phasors).

Similarly, when the applied voltage comprises two periodic wave forms that have different frequency  $\omega_1$  and  $\omega_2$ , the tunnelling current is given by:

$$i(t) = \frac{1}{2} \sum_{m=-\infty}^{\infty} \sum_{n=-\infty}^{\infty} I(m, n) e^{j(m\omega_1 + n\omega_2)t} \quad (2.2)$$

From this equation it can be seen that the tunnelling current contains several terms at frequencies which are linear combinations with integer coefficients of  $\omega_1$  and  $\omega_2$ . One of this combination will be  $\omega_1 - \omega_2$ , which corresponds to the intermediate frequency.

### 2.2.3 Double sideband (DSB) mixers

In a DSB mixer both the upper and lower sidebands are detected. The unwanted sideband can be suppressed using a filter in front of the receiver resulting in a so-called single sideband (SSB) mixer.

Figure 2.6 shows a block diagram of a so-called single-ended or double-sideband sub-millimeter SIS mixer. The input to the mixer is in this case an (quasi-)optical beam formed by the coupling between the LO and antenna signals, which can be performed through beamsplitter, Martin-Pupplett or pure waveguide techniques. This is collected by a focussing optical element and coupled into the SIS junction, producing an intermediate frequency output which is then amplified and detected.

Two common ways to collect the signal and focus it onto the detector are a horn-waveguide probe or a lens-antenna. In the method using the lens-antenna system quasi-optical coupling is employed. A dielectric lens is used to focus the radiation on a planar antenna mounted on the back of the lens (fig. 2.7). An advantage of this technique is the relative ease of fabrication.

In the waveguide method, the input optical beam is focussed into a horn antenna and passed through a waveguide. The SIS chip is mounted in a substrate channel that crosses this waveguide. A transmission line and impedance transformer then couples the radiation from the waveguide probe to the SIS junction, in which the RF and LO signals are mixed (fig. 2.8). Despite the more laborious fabrication (it becomes more difficult to fabricate as the wavelength decreases), this coupling system is largely used for sub-mm band detection because of the good beam quality. This method of coupling is used in the ALMA Band 9 receivers studied in this thesis. The DSB mixers designed for ALMA Band 9 work in the frequency range from 600 to 720 GHz, with an IF range of 4 to 12 GHz.

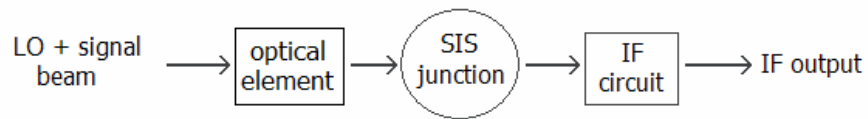


*Figure 2.6: Block diagram of a typical sub-millimeter SIS mixer.*

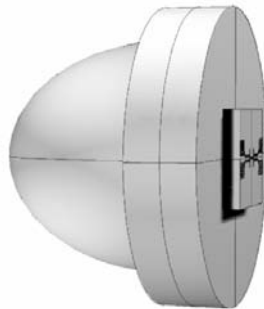


*Figure 2.7: Lens-antenna system.*

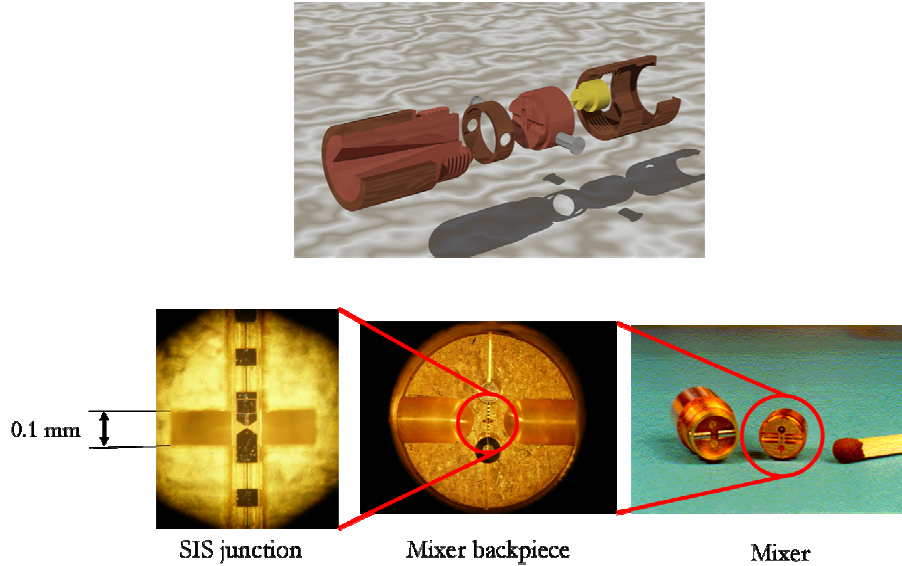


Figure 2.8: DSB mixer used in ALMA Band 9. Upper panel: expanded sketch of the assembly of horn and mixer. The setup comprises the horn (A), the mixer backpiece (B) and the IF output channel (C). Lower panel: structure of the mixer and detail of the SIS junction inside it.

#### 2.2.4 Sideband-separating (2SB) mixers

In 2SB mixers, the unwanted image channel is not filtered out but is separated from the signal channel. The configuration of the 2SB mixer designed as a possible upgrade for ALMA Band 9 is shown in figure 2.9. With the use of a device called a quadrature hybrid, the input RF signal is separated in two parts with a phase difference of  $90^\circ$ . These two signals are then independently combined with an in-phase LO signal and each one is fed into a different SIS junction (DSB). The down-converted signals are sent into another quadrature hybrid. In one output of this hybrid the LSB signal cancels out, while in the other the USB signal cancels out. Thus the USB and LSB signals are obtained separately.

To better explain the working principle of the 2SB mixer, let us consider in detail the scheme of figure 2.9a (see Ref. 14 for similar calculations). As the incoming RF signal passes through the first hybrid, it is split in two parts which have a relative

phase of  $90^\circ$ . We are interested in the components of the RF signal corresponding to the USB and LSB at frequencies  $\omega_U$  and  $\omega_L$ , respectively. These two components arrive with different phases at points A and B in figure 2.9a. At point A, the components have the following time dependence:

$$\begin{aligned} USB &\propto \cos(\omega_U t) \\ LSB &\propto \cos(\omega_L t) \end{aligned} \quad (2.1)$$

while at point B one has:

$$\begin{aligned} USB &\propto \cos(\omega_U t + 90^\circ) \\ LSB &\propto \cos(\omega_L t + 90^\circ) \end{aligned} \quad (2.2)$$

The USB and LSB signals are then down-converted by the DSB mixer with the insertion of the LO signal at frequency  $\omega_{LO}$ . At point C the signals are then:

$$\begin{aligned} USB &\propto \cos(\omega_{LO} t) \cos(\omega_U t) = \cos(\omega_{LO} t) \cos[(\omega_{LO} + \omega_{IF})t] = \frac{1}{2} \cos(\omega_{IF} t) + \frac{1}{2} \cos[(2\omega_{LO} + \omega_{IF})t] \\ LSB &\propto \cos(\omega_{LO} t) \cos(\omega_L t) = \cos(\omega_{LO} t) \cos[(\omega_{LO} - \omega_{IF})t] = \frac{1}{2} \cos(\omega_{IF} t) + \frac{1}{2} \cos[(2\omega_{LO} - \omega_{IF})t] \end{aligned} \quad (2.3)$$

Only the first term after the last equal sign is considered. At point D, in a similar manner, the signals are:

$$\begin{aligned} USB &\propto \cos(\omega_{LO} t) \cos[(\omega_{LO} + \omega_{IF})t + 90^\circ] = \frac{1}{2} \cos(\omega_{IF} t + 90^\circ) + \frac{1}{2} \cos[(2\omega_{LO} + \omega_{IF})t + 90^\circ] \\ LSB &\propto \cos(\omega_{LO} t) \cos[(\omega_{LO} - \omega_{IF})t + 90^\circ] = \frac{1}{2} \cos(\omega_{IF} t - 90^\circ) + \frac{1}{2} \cos[(2\omega_{LO} - \omega_{IF})t + 90^\circ] \end{aligned} \quad (2.4)$$

At point E after the second hybrid, the sidebands from point C are combined with the sidebands at point D delayed by  $90^\circ$ . Thus, the two USB signals are combined with a  $180^\circ$  phase difference (i.e., they are totally out of phase) and therefore cancel out, whereas the LSB signals arrive in phase and are added up:

$$\left[ \frac{1}{2} \cos(\omega_{IF} t) \right]_{USB} + \left[ \frac{1}{2} \cos(\omega_{IF} t) \right]_{LSB} + \left[ \frac{1}{2} \cos(\omega_{IF} t + 180^\circ) \right]_{USB} + \left[ \frac{1}{2} \cos(\omega_{IF} t) \right]_{LSB} \Rightarrow [\cos(\omega_{IF} t)]_{LSB} \quad (2.5)$$

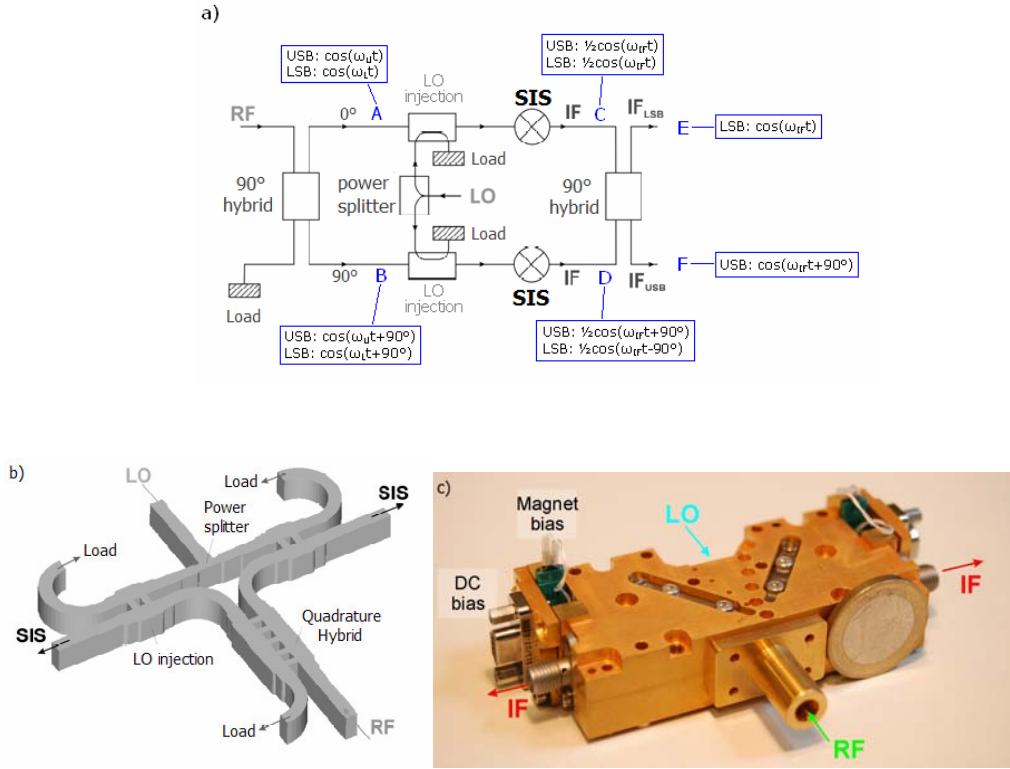


Figure 2.9: a) scheme of the 2SB configuration for ALMA Band 9, b) three-dimensional scheme of the 2SB mixer core (after Ref. 14), c) picture of the 2SB mixer for ALMA Band 9.

In the same way, at point F the LSB signals arrive with a  $180^\circ$  phase difference and cancel each other, while the USB components are combined in-phase:

$$\begin{aligned}
 & \left[ \frac{1}{2} \cos(\omega_{IF} t + 90^\circ) \right]_{USB} + \left[ \frac{1}{2} \cos(\omega_{IF} t + 90^\circ) \right]_{LSB} + \left[ \frac{1}{2} \cos(\omega_{IF} t + 90^\circ) \right]_{USB} + \left[ \frac{1}{2} \cos(\omega_{IF} t - 90^\circ) \right]_{LSB} \\
 & \Rightarrow [\cos(\omega_{IF} t + 90^\circ)]_{USB} \quad (2.6)
 \end{aligned}$$

A difficulty with the 2SB mixers are the very small dimensions of some components required at high frequencies. Nevertheless the performance obtained with this design of the mixer is very good and satisfies the ALMA specifications [15].

A reason to prefer 2SB mixers instead of DSB mixers for high resolution spectral line observations in radio astronomy is their enhanced sensitivity. As the sensitivity

of SIS mixers approaches its fundamental limit, the output noise of a DSB receiver is degraded by the atmospheric noise coming into the system through the image band. Even if there is no RF frequency component in the image sideband, the atmospheric noise in this sideband cannot be removed and contributes to the total IF output, thereby affecting the overall sensitivity.

# INSTRUMENTAL SETUP

### 3.1. The Fourier Transform Spectrometer: general description

The Fourier transform spectrometer (FTS) is a Michelson interferometer with a movable mirror. A block diagram of the FTS is shown in figure 3.1. The light from the source is split in two beams by a beamsplitter. One beam is reflected off a fixed mirror and one off a moving mirror which introduces a variable time delay. After the reflection from the mirrors, the beams are recombined coherently at the beamsplitter and detected. The procedure is repeated for different time delays, corresponding to different positions of the moving mirror.

The intensity  $I(\Delta)$  of the recombined beam, as a function of the path difference  $\Delta$ , is the Fourier transform of the product of the spectral distribution of the source, the transmission of the optical medium (air, vacuum) and the spectral response of the detector, as shown below. This means that an FTS can be used either to study the emission from an unknown source (if the detector is broad-band), or the response of an unknown detector (if the source is broad-band), or the transmission of the medium (e.g. filters or window materials) if both are broad-band.

In general, if the light source is monochromatic and is split in two beams of equal intensity, the electric field component of the recombined beam in the interferometer can be written as:

$$E_T = 2E_0 e^{i\omega t} (1 + e^{ik\Delta}) \quad (3.1)$$

where  $\Delta=2x$  is twice the distance  $x$  (see fig. 3.1) of the movable mirror from the zero path difference position, and  $k=2\pi/\lambda$  [16].

The intensity of the recombined beam can be written as:

$$I = |E_T|^2 = E_0^2 [1 + \cos(k\Delta)]. \quad (3.2)$$

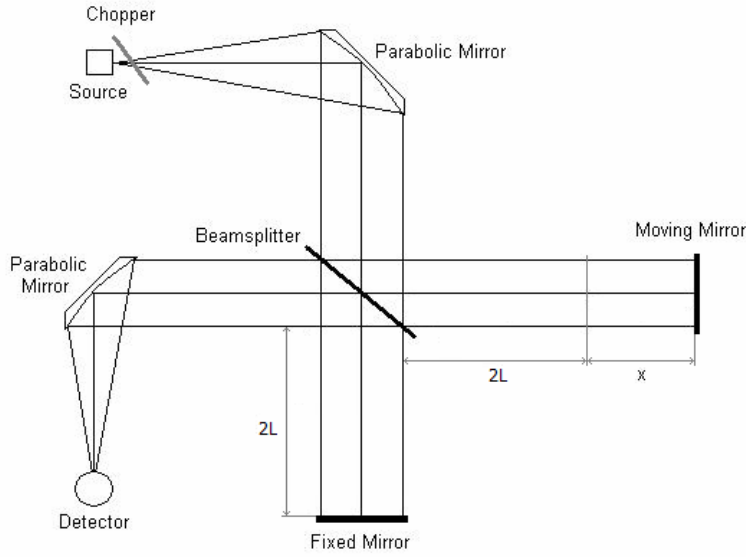


Figure 3.1: Block diagram of the FTS,  $x$  is the distance of the movable mirror from the zero path difference position.

If the light source is not monochromatic, but has a spectral distribution  $S(k)$ , then the intensity of the light from the interferometer can be found by adding the intensities at different wavelengths:

$$I(\Delta) = \int_0^{\infty} |E_T|^2 S(k) dk = \int_0^{\infty} E_0^2 S(k) [1 + \cos(k\Delta)] dk = E_0^2 \left[ I_r + \int_0^{\infty} S(k) \cos(k\Delta) dk \right] \quad (3.3)$$

where  $I_r = \int_0^{\infty} S(k) dk$  is the reference beam.

The integral in the right-hand equation 3.3 is the Fourier cosine transform of  $S(k)$ .

Hence, if we have an interferogram  $\Phi(\Delta) = \int_0^{\infty} S(k) \cos(k\Delta) dk$ , the spectral distribution may be calculated from the Fourier formula considering that  $\Phi(-\Delta) = \Phi(\Delta)$ :

$$S(k) = \frac{2}{\pi} \int_0^{\infty} \Phi(\Delta) \cos(k\Delta) d\Delta \quad (3.4)$$

Since  $\cos(k\Delta)$  is an even function, the interferogram should be symmetrical about the white light fringe ( $\Delta=0$ ) for a perfectly aligned instrument.

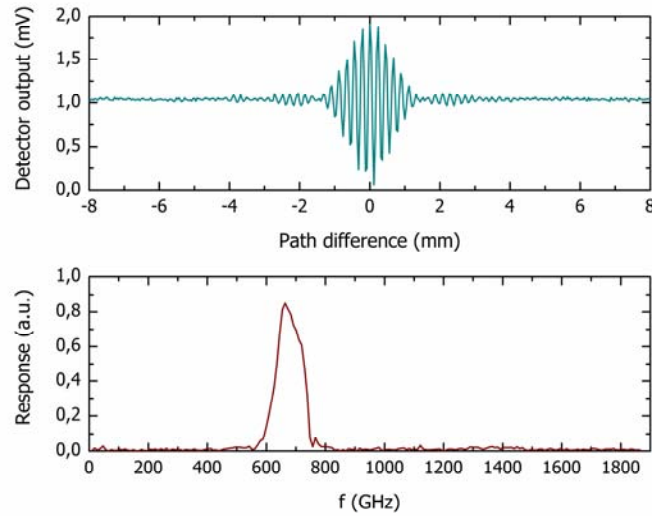


Figure 3.2: Example of interferogram (above) with the correspondent frequency spectra (below) measured by the Michelson interferometer described in this thesis.

An example of interferogram, with the correspondent frequency spectrum, measured by the Michelson interferometer is shown in figure 3.2.

Because the resolution of an FTS increases with increasing optical path difference, the maximum spectral resolution,  $\Delta\nu = \frac{c}{2x_{\max}}$ , is achieved by using the entire

distance to measure one side of the interferogram. However, in order to maximize the signal-to-noise ratio and to avoid problems with cutting of the interferogram, both sides of the interferogram are usually measured. The maximum frequency of

the spectral distribution is given by  $\nu_{\max} = \frac{c}{4s}$ , where  $s$  is the step size of the movable mirror.

The orientation of the mirrors is a critical point: the movable and the fixed mirrors must be exactly perpendicular with respect to the incident beam. A misalignment can produce a reduction in the spectral amplitude and cause asymmetries in the interferogram [17]. For alignment purposes, the source can be replaced by a laser and the detector by a screen.

### 3.2. Instrumental setup for double sideband mixers

A block diagram and a picture of the instrumental setup used during the experiment with the double sideband mixers is shown in figure 3.3. The source consists of a glowbar lamp (black body source) with a chopper in front of it for lock-in measurements (see section 3.2.2). The first part of the setup consists of a Michelson interferometer described in section 3.1.

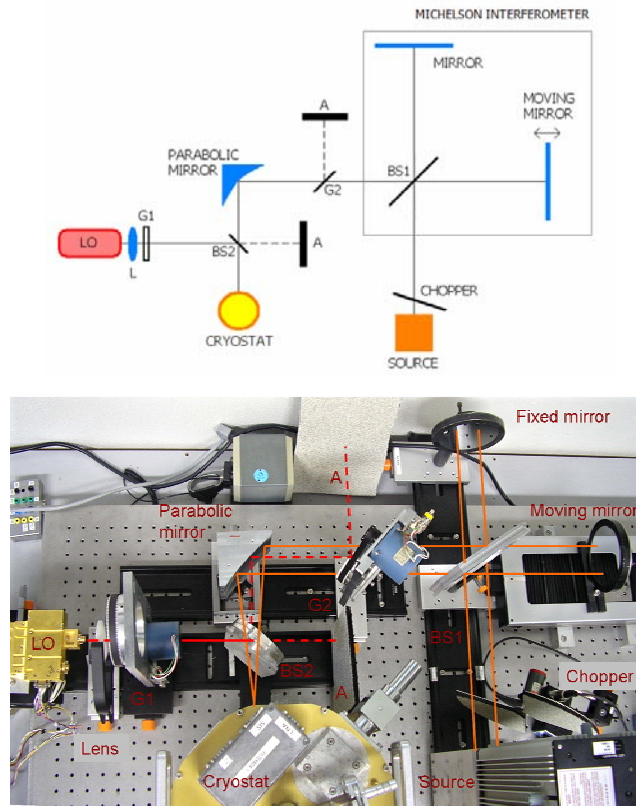


Figure 3.3: Upper panel: scheme of the heterodyne detection setup used with the double sideband mixers. BS1 is the beamsplitter of the Michelson interferometer. The beam from BS1 is coupled with the signal from the LO through beamsplitter BS2. L and G1 are respectively a lens and a grid used to focus and adjust the amplitude of the LO signal. The grid G2 is used to reduce the standing waves from the LO as discussed in the text. The rejected beams are sent to two absorber plates (A). Lower panel: picture of the instrumental setup.

In the Michelson interferometer used during this thesis, the maximum spectral resolution achievable is 750 MHz, corresponding to a difference in path length of 400 mm (or a maximum mirror travel of 200 mm).

When the receiver is used in direct detection mode, the recombined beam is sent to a parabolic mirror (a description of the mirror design is presented in section 3.2.3) which focuses it into the cryostat where the receiver is located. In this way it is possible to obtain the frequency response of the receiver. In heterodyne detection mode, the beam from the parabolic mirror is coupled with the signal from the local oscillator using the beamsplitter BS2. The working principle of the LO is presented in section 3.2.1.

Due to imperfections in the coupling between the incoming signal and the horn receiver, some LO signal can be reflected back into the Michelson interferometer forming standing waves. Since the LO signal is polarized, introducing a new grid (G2) suitably oriented can reduce these standing waves by acting as an adjustable attenuator.

### **3.2.1 Local oscillator**

The local oscillator is an important part of the heterodyne receiver. It is a device used to generate a signal which is mixed against the signal of interest to convert it down to a lower frequency. The LO signal must be coherent and with a high enough power level (several  $\mu\text{W}$ ) in order to adequately pump the mixer. The band coverage, the tuneability and the spectral purity of the LO are also important parameters of a heterodyne system. For our experiments we used a multiplier chain local oscillator. In this device, harmonics generators are used to convert a low frequency signal (generated by a YIG oscillator or a signal generator) to the desired frequency range. In our case the low frequency range was between 16 and 20 GHz, and the total multiplication factor was 36 (two doublers and two triplers in series), producing an LO with a range of about 600 to 720 GHz. This corresponds to ALMA Band 9. Figure 3.4 shows a picture of the LO used for the experiments.

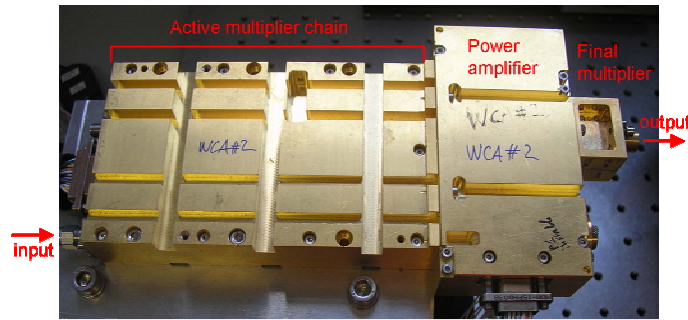


Figure 3.4: Picture of the local oscillator used during the experiments produced by NRAO.

### 3.2.2 Lock-in amplifier

The lock-in amplifier is used to measure the amplitude and phase of signals buried in noise. The principle behind a lock-in amplifier is that the quantity to be measured is modulated and the response is synchronously detected with a very narrow bandwidth around the carrier. In this way both white noise (because of the narrow bandwidth) and  $1/f$  noise (because we stay far away from DC) are greatly reduced.

For measurements in which light is detected, the device used to modulate the signal is usually a chopper. In essence a lock-in amplifier takes the input signal (that corresponds to the detector output signal), multiplies it by the reference signal (provided by the chopper) and integrates it over a specified time. The resulting signal is a DC signal in which the contribution from any signal that is not at the same frequency of the chopper is reduced practically at zero. The integration time of the lock-in is determined in order to obtain the best signal to noise ratio, while keeping the measurement time within reasonable limits. To get sufficient accuracy, the time during which the mirror is kept at a fixed position between two consecutive steps should be at least three times the integration time constant.

### 3.2.3 Design of the parabolic mirrors

During our experiments we made use of a glowbar lamp as source. Because the beam from the lamp is convergent, a mirror is needed to convert it into

approximately a parallel beam in order to feed it into the Michelson interferometer. To this purpose, we have designed a convex parabolic mirror. The beam aperture of the lamp, which already includes an elliptical mirror, is 80 mm. The designed mirror has a focal length of 190 mm and dimensions of 70x70x70 mm. A sketch of the design is shown in figure 3.5.

We have also designed a concave parabolic mirror which couples the beam from the Michelson interferometer into the horn and then into the SIS junction. The horn has a  $f$ -number which is related to the diverging angle of its beam. The aperture ( $a$ ) of the ALMA horn is about  $f/3$ , which means that  $a/f = 1/3$  (see fig. 3.5). As a consequence, because the width of the beam coming from the convex parabolic mirror is approximately 50 mm, the focal length of the mirror should be 150 mm. Due to diffraction effects because of the finite beam size, as well as imperfections of the convex mirror, the beam can be not perfectly parallel. To ensure that the whole beam coming from the convex parabolic mirror is reflected to the horn, the dimensions of the mirror (100x100x100 mm) are oversized (see fig. 3.5).

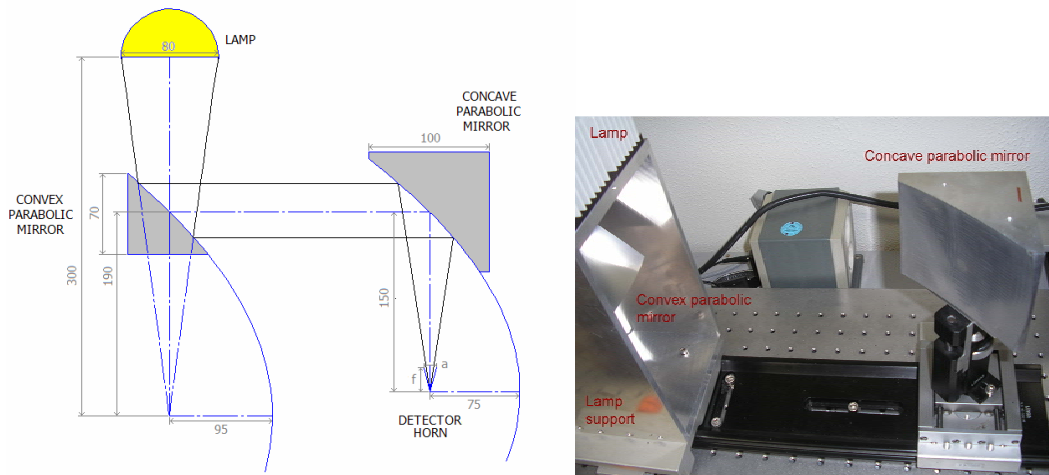


Figure 3.5: Left: sketch of the design of the convex parabolic mirror and the concave parabolic mirror. The converging beam from the lamp is converted into a parallel beam using a convex mirror and then it is focused into the detector using a concave mirror (the dimensions are in mm). Right: picture of the mirrors. The convex parabolic mirror is mounted on the support of the glowbar lamp.

### 3.3. Instrumental setup for sideband-separating mixers

A block diagram and a picture of the instrumental setup used for the experiments with the sideband separating mixers are shown in figure 3.6.

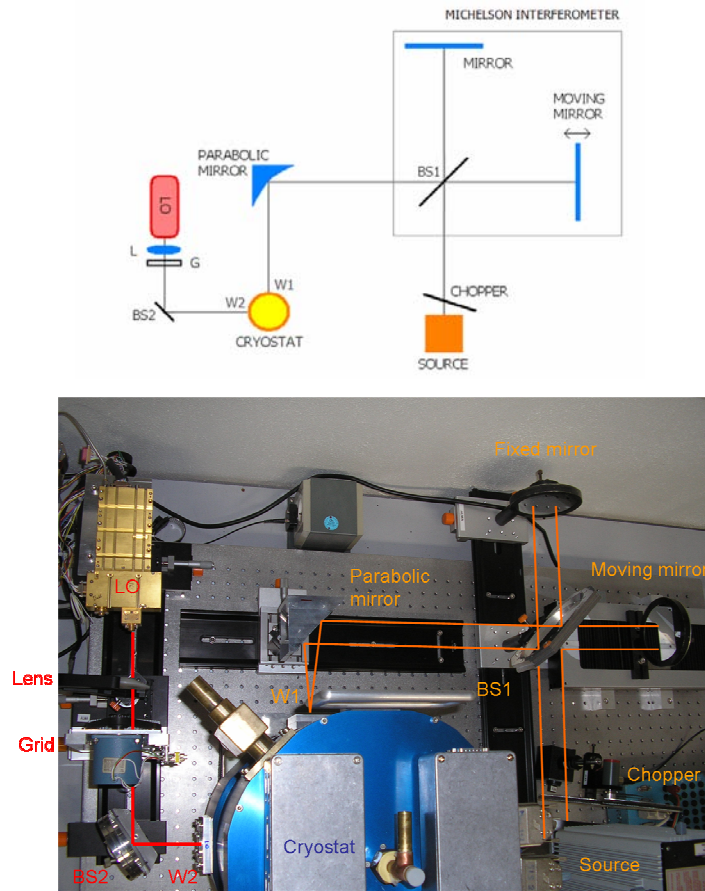


Figure 3.6: Upper panel: scheme of the heterodyne detection setup used with the sideband separating mixers. BS1 is the beamsplitter of the Michelson interferometer. The beam from BS1 is inserted into the cryostat through the window W1. The beam from the LO source is inserted into the cryostat through the window W2. The use of the beamsplitter BS2 allows the alignment of the LO beam without moving the cryostat. L and G1 are respectively a lens and a grid used to focalize and change the amplitude of the LO signal. Lower panel: picture of the instrumental setup.

The difference between this setup and the setup used for the double sideband mixers reflects the different way of operation of the two types of mixers. The cryostat used with the 2SB mixer is equipped with two windows (W1 and W2) for the separate insertion of the input signal and the LO signal, because the mixing between the two signals is done inside the mixer block in the cryostat. Hence the signal from the LO is sent through the window W2 using the beamsplitter BS2 as a simple mirror. The LO signal is not sent directly to the cryostat because in this way it is possible to align the LO beam without moving the cryostat (which is previously aligned with the reference beam inserted through the window W1). Since in this case we use a sideband separating mixer, we have two distinct output signals, one corresponding to the upper side band and the other to the lower sideband. Both signals are detected independently (by using two separate lock-in amplifiers locked to the same reference) in the same way described for the double sideband mixers (see section 3.2).



# SIDEBAND RATIO OF DOUBLE SIDEBAND MIXERS

The purpose of the experiments presented in this chapter is the study of the relation between the direct and heterodyne detection modes to determine if the simple direct detection method is a reliable predictor of the sideband ratio of double sideband mixers.

### 4.1 Detection with double sideband mixers

The measurements described in this chapter were performed in both direct and heterodyne detection modes using two different superconductor-insulator-superconductor (SIS) junctions, hereafter called mixer 1 and mixer 2. Both junctions are designed to operate in the 600–720 GHz band.

#### 4.1.1 Direct detection measurements

For both direct and heterodyne detection mode (see section 3.2 for the description of the instrumental setup), the same cryostat filled with liquid helium (4K) can be used. After the filling of the cryostat the junction is checked by measuring its I-V curve. The measured curves for mixer 1 and 2 are reported in figure 4.1. Josephson currents are suppressed with the application of a magnetic field. For both detection modes, the bias voltage is set to the voltage just before the onset of the jump to normal resistance, namely around 2.5 V (blue points in fig. 4.1).

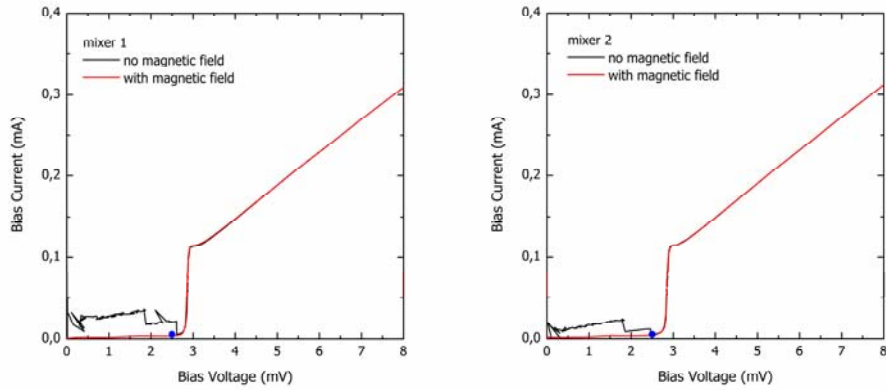


Figure 4.1:  $I$ - $V$  curve of mixer 1 (right) and mixer 2 (left). The red line corresponds to the  $I$ - $V$  curve with the application of a magnetic field to suppress the Josephson effects visible in the black line. The blue point corresponds to the set of the bias voltage (2.5 mV).

For a good experiment the mixer beam should be carefully aligned with the beam from the Michelson interferometer. This is done by manually moving the cryostat in order to find the point at which the intensity of the detected signal is maximum. When the right alignment is found, the response of the mixer can be measured over the entire frequency range using the direct detection mode.

This procedure is used to acquire the direct response of mixers 1 and 2. For the detection of the direct spectrum in mixer 1 a maximum length path difference of the FTS of 16 mm (equal to double of the maximum mirror travel) is used, which gives a resolution of 18.75 GHz; for mixer 2 the resolution is improved to about 9 GHz by increasing the length path difference to 32 mm. This also results in an increase of number of points of the direct spectrum, which allows a better estimate of the area under the curve for the evaluation of the SBR in direct mode and a better signal to noise ratio. The results are shown in figure 4.2. It can be seen from this figure that the detectors are lightly high-tuned with respect to the frequency band of interest (between 600 and 720 GHz). This does not affect our experiments. The fact that the maximum output in the response of mixer 1 differs from that of mixer 2 is not necessarily a feature of the mixers, but may also depends on how precisely the alignment of the system is done and the precise temperature of the glowbar.

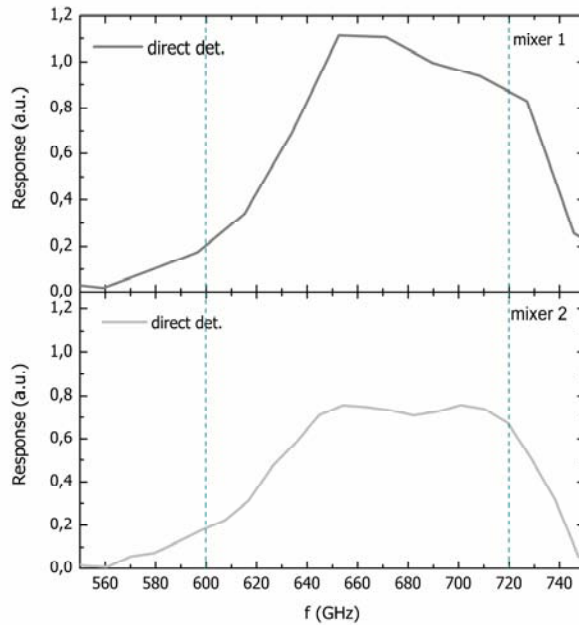


Figure 4.2: Direct response spectrum of mixer 1 and mixer 2.

#### 4.1.2 Heterodyne detection measurements: mixer 1

The configuration for the heterodyne detection is the same as for direct detection but with the insertion of the LO as shown in figure 3.3. No further alignment of the cryostat was performed after the acquisition of the direct spectrum. Before measuring, the LO must be aligned in order to optimize the coupling of the LO signal with the reference signal. First the LO is aligned using a mirror in place of the beamsplitter BS2. Moving the LO source, the mirror, the lens and the grid in front of the LO source, it is possible to find a position in which the pumping level of the junction is maximum. This position can be further adjusted using the beamsplitter BS2. During heterodyne detection, the LO frequency is varied from 597.6 GHz to 720 GHz in steps of 3.6 GHz. A spectrum is taken for every LO frequency. For these measurements we have used a path length difference of 300 mm in order to have a spectral resolution of 1 GHz. Examples of heterodyne spectra acquired with different LO frequencies are shown in figure 4.3. In each spectrum two peaks can be clearly distinguished around the LO frequency. These correspond to the LSB and USB bands.

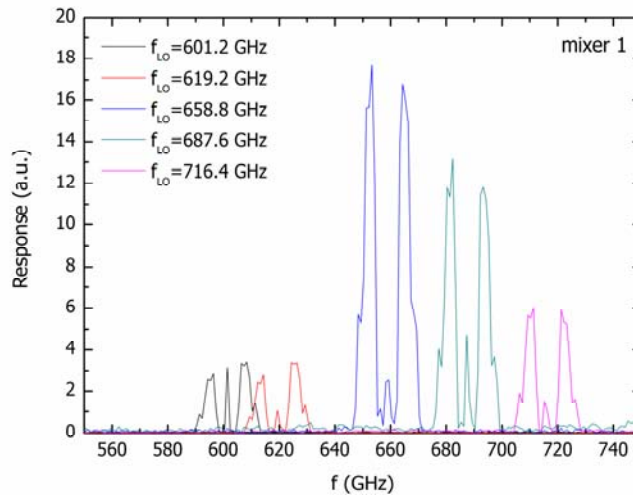


Figure 4.3: Some heterodyne detection spectra at different LO frequencies for mixer 1 as measured.

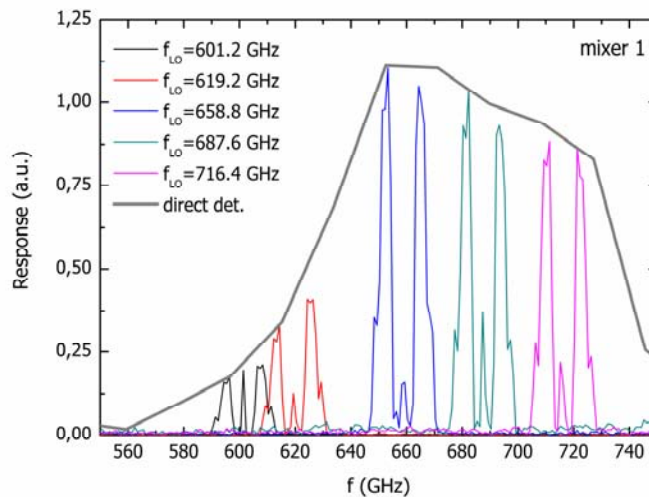


Figure 4.4: Comparison between the direct response spectrum (thick grey line) and some heterodyne detection spectra at different LO frequencies (thin lines) with mixer 1. The spectra are normalized so that the intensity of one of the two sidebands peaks coincides with the intensity of the direct response at the same frequencies.

A third peak is visible between the two main features at exactly the LO frequency. This peak is originated by the standing waves from the LO that are reflected back in the interferometer, causing periodic variations in the pumping level. This means that this configuration of the setup was not optimal.

Since the gain of the mixer and the LO power, and possibly the coupling, is not the same for measurements at different LO frequencies, each of the heterodyne spectra can be normalized so that the intensity of one of the two sideband peaks coincides with the intensity of the direct response at the same frequency. This normalization does not compromise the SBR results, because we are interested in the peak ratio. With this procedure we can directly compare the full spectrum obtained in the direct detection mode with the heterodyne spectra at different LO frequencies. As it can be seen in figure 4.4, the intensity ratio between the upper and lower sideband peaks follows approximately the intensity profile of the direct spectrum.

#### **4.1.3 Heterodyne detection measurements: mixer 2**

From the heterodyne spectra detected with the mixer 1 some problems in the instrumental setup are present. Due to imperfections in the coupling between the incoming signal and the horn receiver, part of the LO signal can be reflected back into the Michelson interferometer forming standing waves. The insertion of grid G2 (see figure 3.3) almost completely solves this problem. Another problem is the low pumping level of the LO at certain frequencies. An example of this is the lack of results between 620 and 640 GHz: the pumping level was not enough to generate a signal response at these frequencies. To overcome this difficulty, we have split the frequency range in two subranges, a low-frequency range from 590.4 GHz to 662.4 GHz and a high-frequency range from 666.0 GHz to 720 GHz. For each range we changed the intensity of the LO beam by rotating the grid G1, in order to optimize the pumping level. We performed a second set of measurements, with mixer 2, where these two changes were implemented. The results are shown in Fig. 4.5. It is evident that the intensity of the central peak in each heterodyne spectrum is lower and we covered all the frequency range with the heterodyne spectra.

Also with this new configuration of the instrumental setup, the spectra taken in the heterodyne mode follow quite well the direct response of the mixer 2 (fig. 4.6). The

same normalization procedure described in the previous subsection was employed here.

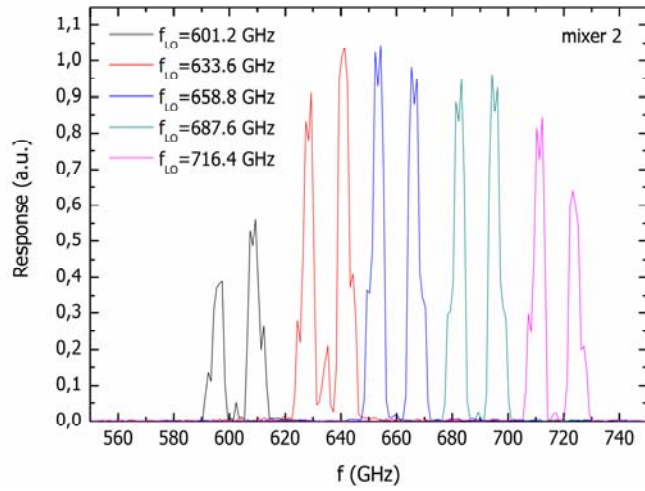


Figure 4.5: Some heterodyne detection spectra, as measured, at different LO frequencies for mixer 2 and with the insertion of the grid G2 in the instrumental setup.

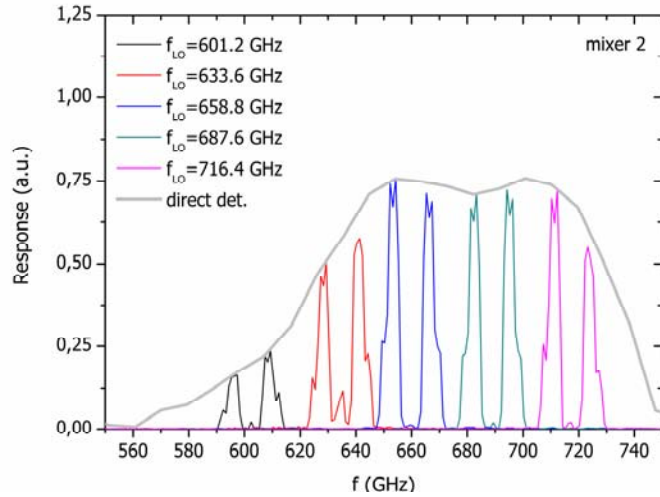


Figure 4.6: Comparison between the direct response spectrum (thick grey line) and some heterodyne detection spectra at different LO frequencies (thin lines) with mixer 2 and with the insertion of the grid G2 in the instrumental setup.

## 4.2 Sideband ratio calculation

### 4.2.1 SBR results

The sideband ratio (SBR) is calculated for each LO frequency as the ratio between the integrals of the USB and LSB peaks ( $I_1$  and  $I_2$  respectively in figure 4.7a). This is then compared with the SBR estimated from the direct detection response, defined as the ratio between the integrals of the direct-detection curve in the same frequency ranges of the USB and LSB peaks, respectively ( $I'_1$  and  $I'_2$  in figure 4.7b).

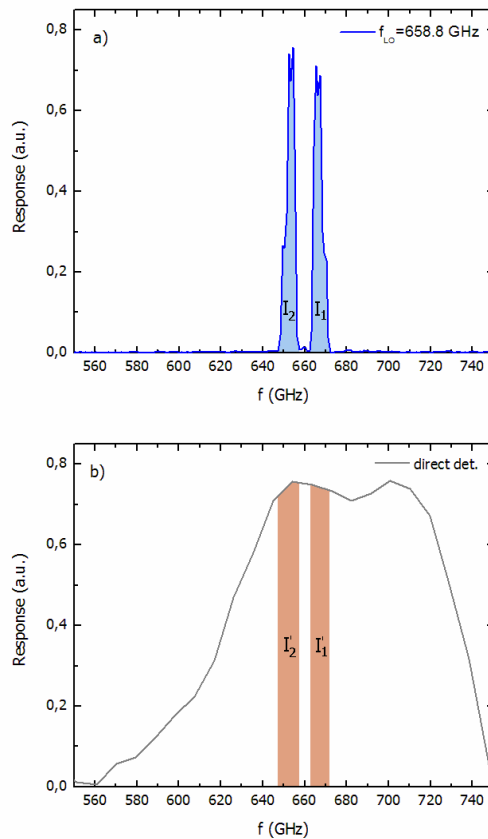


Figure 4.7: a) Area below the USB ( $I_1$ ) and the LSB ( $I_2$ ) peaks in a heterodyne spectra. The SBR is the ratio between these two areas, calculated as numerical integrals, ( $I_1/I_2$ ). b) Areas below the direct detection curve in the same frequency range of  $I_1$  and  $I_2$ . The SBR is defined as the area (integral) ratio  $I'_1/I'_2$ .

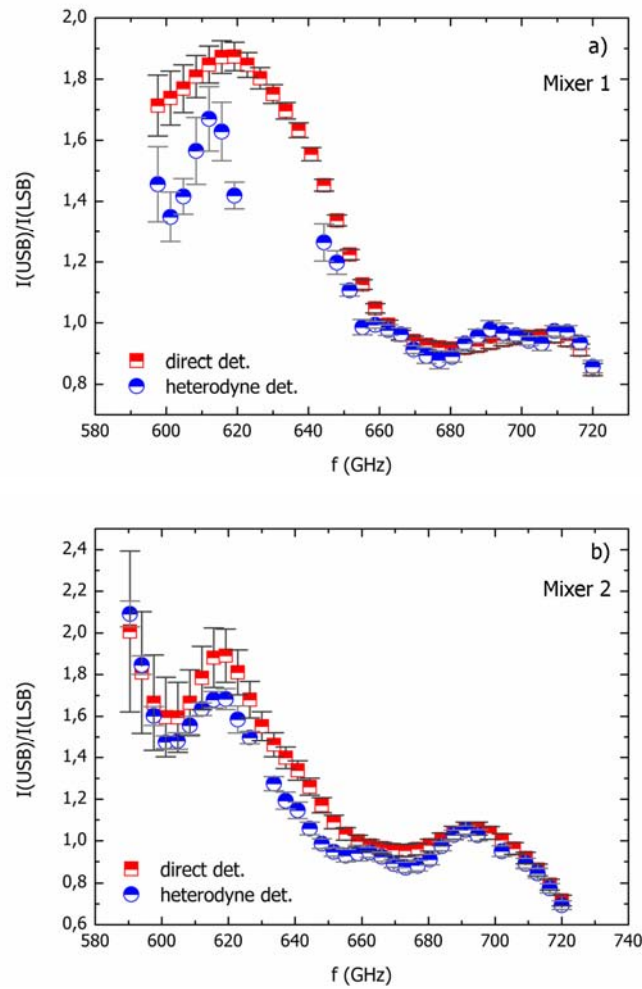


Figure 4.8: Comparison between the measured SBR in heterodyne mode (ratio between the integrals of the USB and LSB peaks) and the estimated SBR from the direct detection response (ratio between the integrals of the direct detection curve in the same frequencies range of the USB and LSB peaks): a) with mixer 1, b) with mixer 2.

The result of this comparison for mixer 1 and 2 is reported in figure 4.8. Each estimate is accompanied by the corresponding error bar (see Appendix A for the error calculation).

#### 4.2.2 Discussion of the results

It can be noted that for both detection modes and for both mixers, the SBR is in the expected range, *i.e.*, between 0.5 and 2.0 [18] (corresponding to  $\pm 3\text{dB}$ ) over the whole frequency range.

From the results obtained with mixer 1 (see fig. 4.8a) it is seen that there are some differences between the SBR in the two different detections modes at frequencies below 640 GHz. The main reason for this is the presence of standing waves coming from the LO source causing the pumping level to change with the position of the moving mirror in the Michelson interferometer. This effect is more pronounced at low frequencies since the coupling between the horn and the incoming signal is also lower at these frequencies, so that the mixer is under-pumped and it is more susceptible to LO power variations. With the changes in the instrumental setup, as discussed in the section 4.1.3, and using mixer 2, a better agreement is found between the two SBR estimates. The two curves in figure 4.8b have qualitatively the same shape. However, also when the noise error bars are considered, there is a quantitative discrepancy in the frequency range between 615 and 660 GHz. This discrepancy is always less than 16% as shown in figure 4.9. Hence the direct detection can be used, at least in the case of the mixer 2, to predict the SBR if an accuracy of 16% is sufficient.

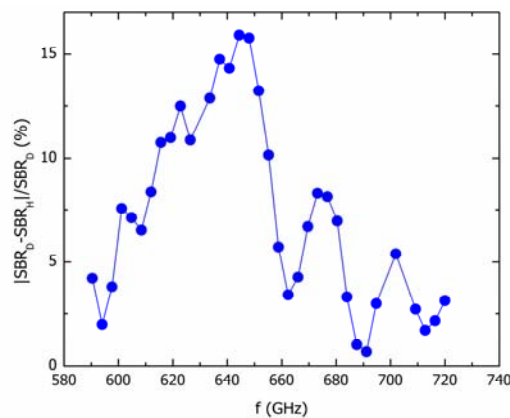


Figure 4.9: Discrepancy (in %) between the SBR calculated from the heterodyne and direct detection for mixer 2.

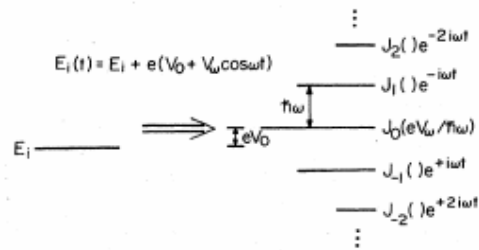


Figure 4.10: Effective splitting of the  $i$ -th quasiparticle level (of unperturbed energy  $E_i$ ) of an ungrounded superconductor in the presence of a AC applied voltage. A microwave field impinging on the superconductor acts as an AC voltage.

More statistics is needed, using different mixers, to give a more reliable estimate for the discrepancy. We estimate however that an accuracy of the order of 20% is a reasonable assumption.

The main reason for the discrepancy is presumably that the heterodyne and direct detection modes are physically different. In particular, the heterodyne detection is based on the non-linear mixing of two signals, while in the direct mode only the source signal is present. The discrepancy may also be caused by other factors, such as the embedding impedance and the mixer impedance, both of which depend on the frequency and pumping level (close to zero in the case of the direct detection). In the following, we analyze in particular the difference between the output DC current in the direct and heterodyne modes [19].

A (weak) microwave field impinging on a junction in which one of the two superconductors is grounded, acts as an AC voltage applied to the ungrounded side of the junction. This sinusoidal perturbation effectively splits each quasiparticle level in the superconductor into a superposition of (virtual) levels separated by multiples of the photon energy  $\hbar\omega$  (see fig. 4.10), occurring with a probability amplitude  $J_n(eV_\omega/\hbar\omega)$ , where  $J_n$  is the Bessel function of order  $n$ . Hence the DC tunnelling current  $I_0$  in the direct detection mode is the sum over the possible tunnelling processes from the grounded superconductor to each of the resulting levels. This is given by the expression:

$$I_0(V_0, V_\omega) = \sum_{n=-\infty}^{\infty} J_n^2\left(\frac{eV_\omega}{\hbar\omega}\right) I_{DC}\left(V_0 + \frac{n\hbar\omega}{e}\right) \quad (4.1)$$

where  $V_0$  and  $V_\omega$  are respectively the DC bias voltage and the AC voltage due to the microwave source.  $I_{DC}(V)$  represents the unpumped DC I-V characteristic of the junction, so that  $I_{DC}(V_0+n\hbar\omega/e)$  is the tunnelling current into the  $n$ -th level. In an analogous way the AC part  $I_\omega$  of the mixer output can be calculated. We are only interested in the DC part.

In the heterodyne mode we have to consider also the strong signal from the LO. The IF is so low that the mixing element sees the same high-frequency RF circuit at the signal and LO frequencies. Therefore the source signal can be considered as a small differential change in the applied LO waveform, and the generated IF amplitudes can be considered as small differential changes in the DC current and voltage. The effect of this signal along with the LO is to produce a small modulation  $dI_0$  of the DC output current  $I_0$  (and similarly for the AC component of the output):

$$dI_0 = \frac{\partial I_0}{\partial V_0} dV_0 + \frac{\partial I_0}{\partial V_\omega} dV_\omega = G_{00}dV_0 + G_{0\omega}dV_\omega. \quad (4.2)$$

The small IF current amplitude is equal to  $dI_0$  in the presence of a fixed bias voltage. The output current in the heterodyne mode is thus:

$$I_{IF} = dI_0|_{V_{DC}} = \frac{G_L G_{0\omega}}{G_L + G_{00}} dV_\omega \quad (4.3)$$

where  $G_L$  is the output load conductance and  $G_{00}$  and  $G_{0\omega}$  are the differential conductances given by:

$$\begin{aligned} G_{00} &= \frac{\partial I_0}{\partial V_0} = \sum_{n=-\infty}^{\infty} J_n^2\left(\frac{eV_\omega}{\hbar\omega}\right) \frac{dI_{DC}(V_0 + n\hbar\omega/e)}{dV_0} \\ G_{0\omega} &= \frac{\partial I_0}{\partial V_\omega} = \frac{e}{\hbar\omega} \sum_{n=-\infty}^{\infty} J_n\left(\frac{eV_\omega}{\hbar\omega}\right) J_{n+1}\left(\frac{eV_\omega}{\hbar\omega}\right) \{I_{DC}[V_0 + (n+1)\hbar\omega/e] - I_{DC}(V_0 + n\hbar\omega/e)\} \end{aligned} \quad (4.4)$$

In the last expression we have used the definition of  $G_{00}$  and  $G_{0\omega}$  and the equation 4.1 for  $I_0$ . It is seen that the output current has a different expression in the two detection modes, as in the heterodyne mode the IF current is the differential increment of the direct-mode output current  $I_0$  with respect to the modulation of the LO signal due to the RF signal.

To quantitatively understand the origin of the measured discrepancy between the direct and heterodyne detection mode, it would be necessary to use a model which takes into account all the above-mentioned factors, including a numerical simulation of the expected output currents with equations (4.1) and (4.3).

### **4.3 Conclusions**

Despite a qualitative agreement, a quantitative discrepancy is found between the SBR calculated from the direct detection and heterodyne detection modes in the frequency range between 615 and 660 GHz, which can be only partially reduced by suppressing the LO standing waves in the heterodyne mode. With the improved setup, the discrepancy between the SBR calculated from the direct and heterodyne spectra of mixer 2 is always less than 16%. We can reasonably assume that, in general, the direct detection can be used to predict the SBR if an accuracy of 20% is sufficient. More experiments are needed to obtain a more reliable estimate for the SBR discrepancy, accompanied by simulations to understand in detail its causes, which might be mainly related to the physical non-equivalence between the two detection techniques and to the different detector response in the two cases.

# SIDEBAND RATIO OF SIDEBAND-SEPARATING MIXERS

In the case of sideband-separating mixers, the sideband ratio is the ratio between the intensity of the passed band and the rejected band, also called the “image rejection”. In the ideal case the image rejection is infinite. The standard method to calculate the image rejection in sideband-separating mixers is rather complicate (see section 5.1), thus we will try to compare the image rejection of sideband-separating mixers calculated with such method with the image rejection calculated using heterodyne spectra measured with a Michelson interferometer.

### **5.1 Description of the standard method**

The standard technique used to calculate the SBR for sideband-separating mixers involves the injection of a continuous wave (CW) signal of known relative amplitude into the upper and lower sidebands, and measuring the IF response to each. At millimeter wavelength, however, it is difficult to determine with sufficient accuracy the relative amplitude of two low level RF signals. To overcome this problem, it is possible to measure the SBR of a sideband-separating mixer without knowledge of the RF signal levels, by measuring the IF response to broadband RF noise sources at two distinct temperatures [10].

Let us consider a sideband-separating receiver in which only the conversion from the upper and lower sideband to the IF band is significant (conversion from higher harmonics is negligible). The scheme of such a receiver is shown in figure 5.1.  $G_{i,j}$  are the conversion gains from each RF input port to each IF output port.

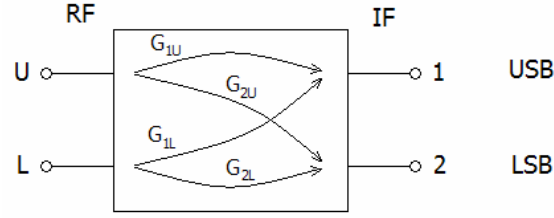


Figure 5.1: Sketch of the sideband-separating receiver.  $G_{ij}$  are the power gains from each RF input port (U and L) to each IF port (1 and 2).

For this receiver the image rejections are:

$$R_{USB} = G_{1U} / G_{1L} \quad \text{at the IF port 1, and} \quad (5.1)$$

$$R_{LSB} = G_{2L} / G_{2U} \quad \text{at the IF port 2.} \quad (5.2)$$

To determine these quantities the following measurements must be performed:

- The IF signals at ports 1 and 2 are measured by applying a CW test signal of unknown amplitude at the upper sideband port U. The ratio of the powers of the two outputs is  $M_U = G_{1U} / G_{2U}$ .
- The IF signals at ports 1 and 2 are measured by applying a CW test signal at the lower sideband port L. The ratio of the powers of the two outputs is  $M_L = G_{2L} / G_{1L}$ .
- By replacing a cold load at the receiver by a hot load, the variation of the output power at the two IF ports is measured. These changes are defined as:

$$\Delta P_1 = k_B \Delta T (G_{1U} + G_{1L}) \quad \text{and} \quad (5.3)$$

$$\Delta P_2 = k_B \Delta T (G_{2U} + G_{2L}) \quad (5.4)$$

where  $\Delta T$  is the noise temperature difference between the two loads. From the measured quantities  $M_U$ ,  $M_L$  and  $M_{DSB} = (\Delta P_1 / \Delta P_2)$  it is possible to calculate the image rejections  $R_{USB}$  and  $R_{LSB}$ :

$$R_{USB} = M_U \frac{M_L M_{DSB} - 1}{M_U - M_{DSB}} \quad \text{and} \quad R_{LSB} = M_L \frac{M_U - M_{DSB}}{M_L M_{DSB} - 1} \quad (5.5)$$

## 5.2 Heterodyne detection measurements

The configuration for the heterodyne detection was shown in figure 3.5. The procedure for the measurements is the same as described for the double sideband receiver in section 4.1.2. The LO frequency is varied from 612 GHz to 693 GHz in steps of 9 GHz, and a mirror travel of 150 mm in the Michelson interferometer is used in order to have a spectral resolution of 1 GHz.

Since the sideband separating mixers have two output signals, two spectra are measured for every LO frequency: one corresponding to the LSB channel and the other to the USB channel. These spectra are shown in figure 5.2. In these first set of measurements some contributions of standing waves at LO frequency are visible.

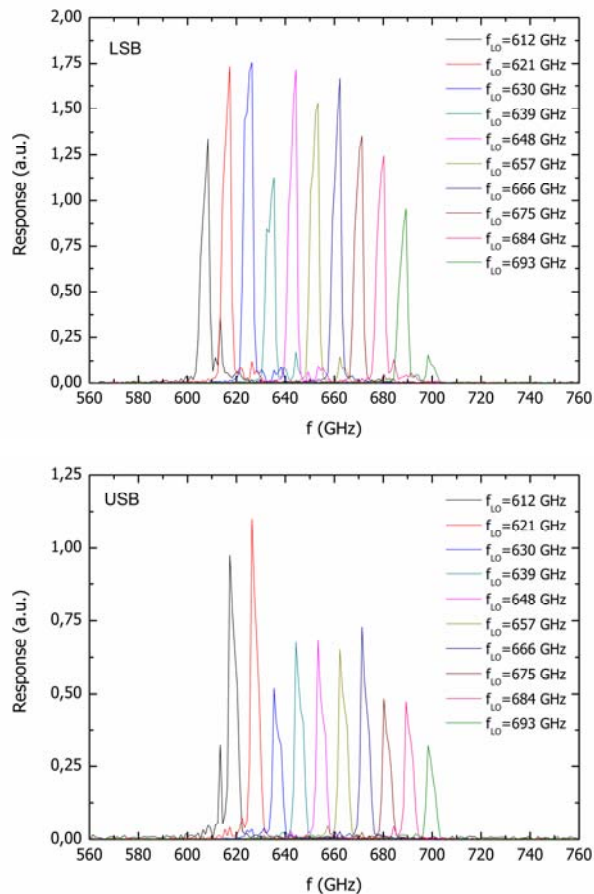


Figure 5.2: Heterodyne spectra of the LSB channel (above) and of the USB channel (below).

These standing waves are presumably an unwanted side effect produced in the coupling between LO and RF inside the mixer block in the cryostat. Referring to figure 2.9a, during LO injection some contribution ( $\sim 1\%$ ) of the LO signal is sent towards the RF port and subsequently in the Michelson path through the window W1. To check if these standing waves from the LO are the cause of the peak at the LO frequency in the heterodyne spectra of our 2SB mixer, an approach could be to put a grid in front of the window W1 and try reducing them by changing the grid polarization. In general these waves can also be generated from leakage and reflections of the LO signal in the cryostat or in the mixer block. In both cases an improvement of the instrumental setup is necessary in order to reduce the central peak in the heterodyne spectra.

### **5.3 Image rejection calculations**

The calculation of the image rejection (R) is similar to the SBR calculations based on the heterodyne spectra for the double sideband receivers. If  $L_1$  and  $U_1$  are respectively the areas below the LSB and USB peaks of the spectrum measured at the LSB channel, its image rejection is defined as  $R_{\text{LSB}}=L_1/U_1$  (see fig. 5.3a). Analogously, the image rejection of the USB channel is defined as  $R_{\text{USB}}=U_2/L_2$ , where  $L_2$  and  $U_2$  are respectively the areas below the LSB and USB peaks in the spectra measured at the USB channel (see fig. 5.3b).

The results of this calculation [15] are shown in figure 5.4 together with the image rejection calculated with the method described by Kerr in Ref. 7. The error on the image rejection is obtained for each heterodyne spectrum with the method described in section 4.3.

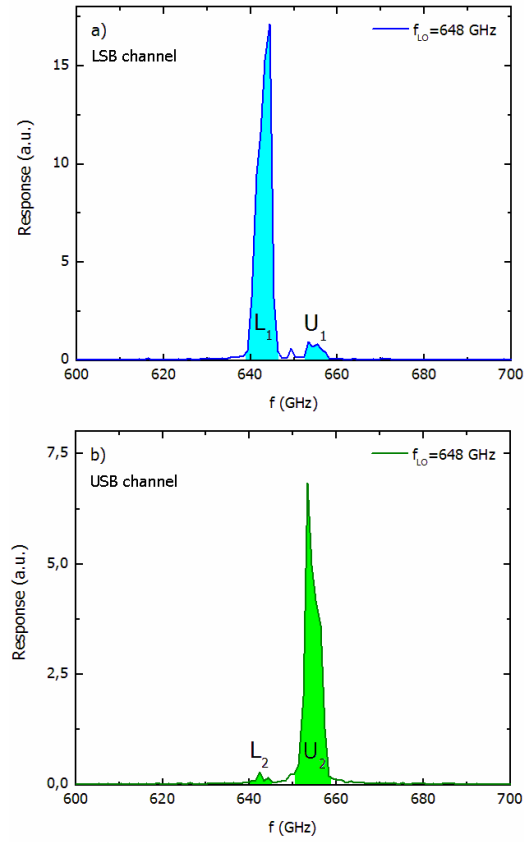


Figure 5.3: Area below the USB and LSB peaks in a heterodyne spectrum obtained from the LSB channel (a) of the sideband-separating mixer and from the USB channel (b). The image rejection for each channel is the ratio between these two areas (calculated as numerical integrals), namely  $R_{LSB}=L_1/U_1$  and  $R_{USB}=U_2/L_2$ .

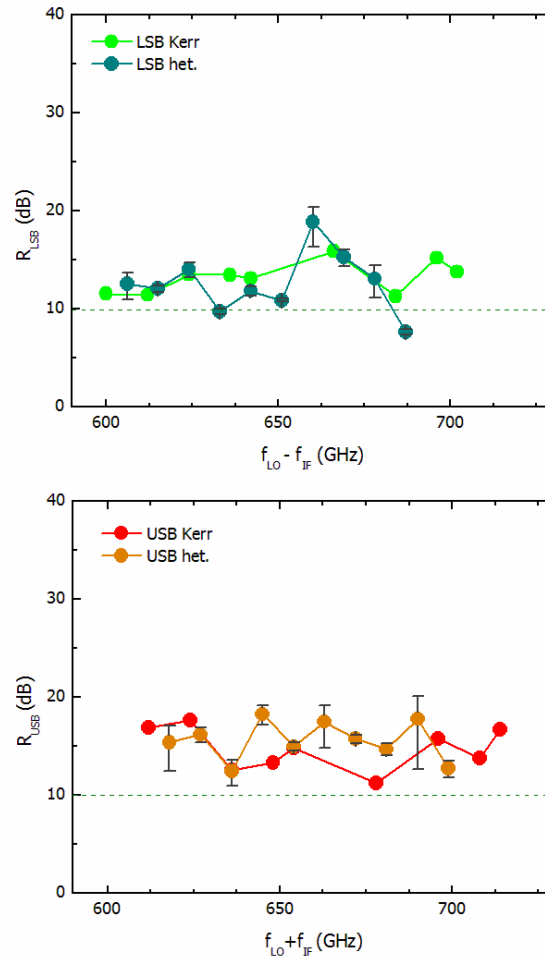


Figure 5.4: Comparison between the image rejection calculated with the method described by Kerr and the image rejection calculated from the heterodyne spectra for both the LSB (above) and the USB (below) channels.

## 5.4 Conclusions

These first results are quite satisfactory, but there are some differences between the image rejections calculated with the two methods. This has probably do to the presence of standing waves at the LO frequency in the signal path. It is therefore necessary to improve the experimental setup to investigate if the standing waves are the cause of the discrepancy and if they can be removed.

## APPENDIX A

---

### SBR ERROR CALCULATION

In the calculation of the error we take into account only the statistical error due to the finite integration time. To calculate the error associated with the calculated SBR, we consider an example of detected spectrum in figure A.1. In general, the integral in the A-B interval can be approximated as:

$$I = \int_A^B f(x)dx \approx \sum_i p_i \Delta x_i$$

where  $p_i$  is the height of the curve at the point  $x_i$  and  $f(x)$  is the curve that interpolates the points  $p_i$ . In our case all intervals  $\Delta x_i$  have the same length  $\Delta x$ . The absolute error  $E(p_i)$  associated with each point  $p_i$  can be assumed to be the same for every point of the curve. An estimate for this error can be obtained by considering the signal maximum in the part of the spectrum which is “spectroscopically empty”. We denote such maximum by  $E_p$  in figure A.1.

In general, the combined uncertainty  $\Delta Y$  of a measurement  $Y = f(x_1, x_2, \dots, x_N)$  is defined as [20]:

$$(\Delta Y)^2 = \sum_{i=1}^N \left( \frac{\partial f}{\partial x_i} \right)^2 (\Delta x_i)^2 + 2 \sum_{i=1}^N \sum_{j=1}^N \frac{\partial f}{\partial x_i} \frac{\partial f}{\partial x_j} \Delta x_i \Delta x_j$$

If the quantities  $x_i$  are uncorrelated, the term containing the partial derivatives vanishes. Hence the total (absolute) error  $E_I$  associated with the value of the integral can be written as:

$$E_I = \sqrt{\sum_i (\Delta x_i E(p_i))^2} = \Delta x E_p \sqrt{n}$$

The SBR is a ratio between two integrals ( $I_1$  and  $I_2$ ), hence the error on the ratio is:

$$E_{SBR} = SBR \sqrt{\left( \frac{E_{I_1}}{I_1} \right)^2 + \left( \frac{E_{I_2}}{I_2} \right)^2} = SBR \sqrt{\left( \frac{\sqrt{n_1} \Delta x E_p}{I_1} \right)^2 + \left( \frac{\sqrt{n_2} \Delta x E_p}{I_2} \right)^2}$$

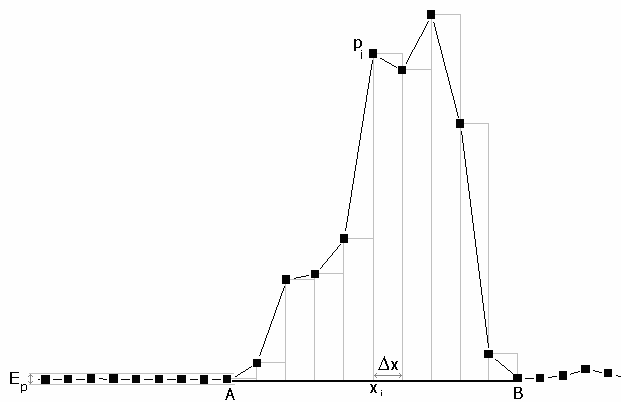


Figure A.1: Example of a detected spectrum.  $p_i$  are the points forming the spectrum,  $\Delta x_i$  the integration sub-intervals and  $E_p$  is the error associated to every point  $p_i$ .

where  $n_1$  and  $n_2$  are the number of sub-intervals in which AB is divided. The value  $n\Delta x$  is the length  $L$  of the integration interval AB, which in our case equals to 8 GHz, corresponding to the IF band. Hence the error associated at the calculated value of the SBR can be written as:

$$E_{SBR} = SBR \sqrt{\left(\frac{L \cdot E_p}{I_1 \cdot \sqrt{n_1}}\right)^2 + \left(\frac{L \cdot E_p}{I_2 \cdot \sqrt{n_2}}\right)^2}.$$

## APPENDIX B

---

### PROGRAMS WITH MATHEMATICA 5.2

#### 1. Calculation of the SBR for double sideband mixers

```
(*SBR heterodyne mode*)

SetDirectory["C:\\DSB\\SBR"];
files = FileNames["*.fts"];
result = {};
intHet1 = {};
intHet2 = {};
ratioDataHet = {};
c = Length[files];
For[i = 0, i <= (c - 1), i++,
  data = Import[files[[i]], "table"];
  n = Dimensions[data];
  s = n[[1]] - 8;
  data = Take[data, -s];
  f = Interpolation[data];
  fLO = (16.30 + i * 0.10) * 36 * 10^9;
  R1 = x /. FindRoot[f[x] == 0.003, {x, fLO - 10 * 10^9}];
  R2 = x /. FindRoot[f[x] == 0.003, {x, fLO - 3 * 10^9}];
  int1 =  $\int_{R1}^{R2} f[x] dx$ ;
  intHet1 = Append[intHet1, int1];
  R3 = x /. FindRoot[f[x] == 0.003, {x, fLO + 5 * 10^9}];
  R4 = x /. FindRoot[f[x] == 0.003, {x, fLO + 13 * 10^9}];
  int2 =  $\int_{R3}^{R4} f[x] dx$ ;
  intHet2 = Append[intHet2, int2];
  ratio = int2 / int1;
  ratioDataHet = Append[ratioDataHet, ratio];
  result = Append[result, {fLO, ratio}];
];
g1 = ListPlot[result, AxesLabel -> {"Hz", ""}, PlotStyle -> PointSize[0.02], PlotRange -> {0, 3},
  DisplayFunction -> Identity];
Export["int1HetD33", intHet1, "list"];
Export["int2HetD33", intHet2, "list"];
Export["ratioHetD33", ratioDataHet, "list"];
Export["ratioHetD33.dat", result];
```

```

(*SBR direct mode*)

SetDirectory["C:\\DSB\\FTS"];

result2 = {};
intDir1 = {};
intDir2 = {};
ratioDataDir = {};
data2 = Import["ftsD33.fts", "table"];
n = Dimensions[data2];
s = n[[1]] - 8;
data2 = Take[data2, -s];
f = Interpolation[data2];
For[i = 0, i <= 36, i++,
  fLO2 = (16.30 + i*0.10) * 36 * 10^9;
  fA = fLO2 - 12 * 10^9;
  fB = fLO2 - 4 * 10^9;
  int1 =  $\int_{fA}^{fB} f[x] dx$ ;
  intDir1 = Append[intDir1, int1];
  fC = fLO2 + 4 * 10^9;
  fD = fLO2 + 12 * 10^9;
  int2 =  $\int_{fC}^{fD} f[x] dx$ ;
  intDir2 = Append[intDir2, int2];
  ratio2 = int2 / int1;
  ratioDataDir = Append[ratioDataDir, ratio2];
  result2 = Append[result2, {fLO2, ratio2}];
];
g2 = ListPlot[result2, AxesLabel -> {"Hz", ""}, PlotStyle -> {Hue[0.5], PointSize[0.02]},
  PlotRange -> {0, 3}, DisplayFunction -> Identity];
g = Show[g1, g2, DisplayFunction -> $DisplayFunction];
Export["ratioDirD33.dat", result2];
Export["int1DirD33", intDir1, "list"];
Export["int2DirD33", intDir2, "list"];
Export["ratioDirD33", ratioDataDir, "list"];

```

## 2. Calculation of the error associated with the SBR of DSB

(\*Error direct mode\*)

```

SetDirectory["C:\\DSB\\FTS"];
data = Import["ftsDSB.fts", "table"];
n = Dimensions[data];
s = n[[1]] - 9;
data = Take[data, -s];
data = Take[data, 48];
Err = Max[data[[All, 2]]];
SetDirectory["C:\\DSB\\errorData"];
files = FileNames["*"];
errorDirect = {};
int1 = Import[files[[1]], "list"];
int2 = Import[files[[3]], "list"];
ratio = Import[files[[5]], "list"];
c = Length[int1];
For[i = 0, i <= (c - 1), i++,
  ErrDir = ratio[[i]] *  $\sqrt{\left(\frac{(8 * 10^9) * Err}{int1[[i]]}\right)^2 + \left(\frac{(8 * 10^9) * Err}{int2[[i]]}\right)^2}$ ;
  errorDirect = Append[errorDirect, ErrDir];
];
Export["ErrorDirectD33.dat", errorDirect];

```

(\*Error Heterodyne mode\*)

```

SetDirectory["C:\\DSB\\SBR"];
error = {};
files = FileNames["*.fts"];
For[i = 0, i <= 36, i++,
  data = Import[files[[i]], "table"];
n = Dimensions[data];
s = n[[1]] - 8;
data = Take[data, -s];
data2 = Take[data, {15, 550}];
Err2 = Max[data2[[All, 2]]];
error = Append[error, Err2];
];

int1 = Import[files[[2]], "list"];
int2 = Import[files[[4]], "list"];
ratio = Import[files[[6]], "list"];
errorHet = {};
c = Length[int1];
For[i = 0, i <= (c - 1), i++,
  ErrHet = ratio[[i]] *  $\sqrt{\left(\frac{(8 * 10^9) * error[[i]]}{int1[[i]] * \sqrt{9}}\right)^2 + \left(\frac{(8 * 10^9) * error[[i]]}{int2[[i]] * \sqrt{9}}\right)^2}$ ;
  errorHet = Append[errorHet, ErrHet];
];
Export["ErrorHeterD33.dat", errorHet];

```

### 3. Calculation of $R_{\text{USB}}$ and $R_{\text{LSB}}$ for sideband-separating mixers

```

SetDirectory["C:\\2SB\\data\\heter"];
filesLSB = FileNames["*.fts"];
filesUSB = FileNames["*.fts2"];
rUSB = {};
rLSB = {};
L1data = {};
U1data = {};
L2data = {};
U2data = {};
rUSBdata = {};
rLSBdata = {};
c = Length[filesLSB];
For[i = 0, i <= (c - 1), i++,
  dataLSB = Import[filesLSB[[i]], "table"];
  dataUSB = Import[filesUSB[[i]], "table"];
  n = Dimensions[dataLSB];
  s = n[[1]] - 8;
  dataLSB = Take[dataLSB, -s];
  dataUSB = Take[dataUSB, -s];
  fLSB = Interpolation[dataLSB];
  fUSB = Interpolation[dataUSB];
  fLO = (16.75 + i * 0.25) * 36 * 10^9;
  fA = fLO - 8 * 10^9;
  fB = fLO - 4 * 10^9;
  fC = fLO + 4 * 10^9;
  fD = fLO + 8 * 10^9;
  L1 =  $\int_{fA}^{fB} f_{\text{USB}}[x] dx$ ;
  U1 =  $\int_{fC}^{fD} f_{\text{USB}}[x] dx$ ;
  L2 =  $\int_{fA}^{fB} f_{\text{LSB}}[x] dx$ ;
  U2 =  $\int_{fC}^{fD} f_{\text{LSB}}[x] dx$ ;
  R1 = U1 / L1;
  R2 = U2 / U2;
  L1data = Append[L1data, L1];
  U1data = Append[U1data, U1];
  L2data = Append[L2data, L2];
  U2data = Append[U2data, U2];
  rUSB = Append[rUSB, {fLO, R1}];
  rUSBdata = Append[rUSBdata, R1];
  rLSB = Append[rLSB, {fLO, R2}];
  rLSBdata = Append[rLSBdata, R2];
];
Export["imrejectionUSB.dat", rUSB];
Export["imrejectionLSB.dat", rLSB];
Export["L1data", L1data, "list"];
Export["U1data", U1data, "list"];
Export["imrejUSBdata", rUSBdata, "list"];
Export["L2data", L2data, "list"];
Export["U2data", U2data, "list"];
Export["imrejLSBdata", rLSBdata, "list"];

```

#### 4. Calculation of the error associated with $R_{USB}$ and $R_{LSB}$

```
(*error USB*)

SetDirectory["C:\\2SB\\heterUSB"];
error = {};
files = FileNames["*.fts2"];
For[i = 0, i < 9, i++,
  data = Import[files[[i]], "table"];
  n = Dimensions[data];
  s = n[[1]] - 8;
  data = Take[data, -s];
  data2 = Take[data, {15, 500}];
  Err = Max[data2[[All, 2]]];
  error = Append[error, Err];
];

SetDirectory["C:\\2SB\\errorData2SB"];
files = FileNames["*"]

L1 = Import[files[[5]], "list"];
U1 = Import[files[[7]], "list"];
rUSB = Import[files[[4]], "list"];
errorUSB = {};
errorInt = {};
For[i = 0, i < 9, i++,
  ErrInt =  $\sqrt{\frac{(4 \times 10^9 * error[[i]])^2}{4}}$ ;
  errorInt = Append[errorInt, ErrInt];
  ErrUSB = rUSB[[i]] *  $\sqrt{ErrInt^2 * \left( \frac{1}{(U1[[i])^2} + \frac{1}{(L1[[i])^2} \right)}$ ;
  errorUSB = Append[errorUSB, ErrUSB];
];
Export["ErrorImRejUSB.dat", errorUSB];
```

```

(*error LSB*)

SetDirectory["C:\\2SB\\heterLSB"];
error = {};
files2 = FileNames["*.fts"];
For[i = 0, i < 9, i++,
  data3 = Import[files2[[i]], "table"];
  n = Dimensions[data3];
  s = n[[1]] - 8;
  data3 = Take[data3, -s];
  data4 = Take[data3, {15, 500}];
  Err = Max[data4[[All, 2]]];
  error = Append[error, Err];
];

SetDirectory["C:\\2SB\\errorData2SB"];
files = FileNames["*"]

L2 = Import[files[[6]], "list"];
U2 = Import[files[[8]], "list"];
rLSB = Import[files[[3]], "list"];
errorLSB = {};
errorInt = {};
For[i = 0, i < 9, i++,
  ErrInt =  $\sqrt{\frac{(4 * 10^9 * error[[i]])^2}{4}}$ ;
  errorInt = Append[errorInt, ErrInt];
  ErrLSB = rLSB[[i]] *  $\sqrt{ErrInt^2 * \left(\frac{1}{(U2[[i])^2} + \frac{1}{(L2[[i])^2}\right)}$ ;;
  errorLSB = Append[errorLSB, ErrLSB];
];
Export["ErrorImRejLSB.dat", errorLSB];

```

## References

---

- [1] H. H. Davè, A. Dubey, S. Thampi, R. P. Singh, “Submillimeter wave science and applications”, in *Proc. of the 28<sup>th</sup> URSI General Assembly, 2005*, available online at: [http://www.ursi.org/Proceeding/ProcGA05/pdf/JB2.4\(0610\).pdf](http://www.ursi.org/Proceeding/ProcGA05/pdf/JB2.4(0610).pdf)
- [2] A. Barychev, “Superconductor-Insulator-Superconductor THz mixer integrated with a superconducting flux-flow oscillator”, *PhD thesis*, Technische Universiteit Delft, (2005).
- [3] T. G. Phillips, “Prospects for high resolution spectroscopy from future space platforms”, in *Proc. of the Far-IR, Sub-MM and MM Detector Technology Workshop* (2002).
- [4] See <http://www.mpifr-bonn.mpg.de/staff/kmenten/APEX-flyer-KMM.pdf>
- [5] S. Payan *et al.*, “A review of remote sensing techniques and related spectroscopy problems”, in *Comptes Rendus Physique*, 6, 825, (2005).
- [6] See <http://www.eso.org/projects/ALMA/specifications/FreqBands.html>
- [7] “Science with ALMA”, available online at: <http://www.eso.org/projects/ALMA/publications/papers/alma-science.pdf>
- [8] K. Kikuchi *et al.*, “Simple FTS measurement system for submillimeter SIS mixer”, *Int. J. IR MM Waves*, 23, 1019, (2002).
- [9] D. Teyssier *et al.*, “A multi-path far-infrared and sub-millimeter gas cell for spectral tests of Herschel/HIFI”, in *Proc. of the 15<sup>th</sup> ISSTT*, 2004, session 7, paper 25.
- [10] A. R. Kerr *et al.*, “Sideband calibration of millimetre-wave receivers”, ALMA Memo 357, available online at: <http://www.alma.nrao.edu/memos/html-memos/alma357/memo357.pdf>
- [11] J. H. Hinken, “Superconductor electronics: fundamentals and microwave applications”, Springer-Verlag (1989).
- [12] J. Bardeen, L. N. Cooper, J. R. Schrieffer, “Theory of superconductivity”, *Phys. Rev.* 108, 1175, (1957).

- [13] S. Withington *et al.*, “Multitone quantum simulations of saturating tunnel junction mixers”, in *J. Appl. Phys.* 93, 9812, (2003).
- [14] V.V. Vassilev, “Development of a sideband separating SIS mixer technology for mm-wavelengths”, *PhD thesis*, Chalmers University of Technology of Göteborg, Sweden, (2003).
- [15] F. P. Mena *et al.*, “Construction of a side-band separating heterodyne mixer for Band 9 of ALMA”, in *Proc. of the 18<sup>th</sup> ISSTT*, 2007.
- [16] J. C. Albergotti, “Fourier Transform Spectroscopy Using a Michelson Interferometer”, in *American J. of Phys.*, 40, 1070, (1972).
- [17] M. Bin *et al.*, “A large throughput high resolution Fourier transform spectrometer for submillimeter applications”, *Int. J. IR MM Waves*, 20, 383, (1999).
- [18] G. H. Tan, “Band 9 Cartridge technical specifications, FEND-40.02.09.00-002-A-SPE”, ESO report, December 2003.
- [19] J. R. Tucker and M. J. Feldman, “Quantum detection at millimeter wavelengths”, in *Rev. of Modern Phys.*, 57, 1055, (1985).
- [20] B. N. Taylor *et al.*, “Guidelines for evaluating and expressing the uncertainty of NIST measurement results”, *NIST Technical Note 1297*, (1994).

## **ACKNOWLEDGEMENTS**

Two years have gone and I am now at the end of my master...at last! There are many people that made this possible, and for this I would like to thank them.

A thank you goes in particular to Prof. Reynier Peletier, who gave me the possibility to attend this new master programme and who has followed my progress during these two years. Thanks to all the “Kapteyner” that I met during this period, and to Umut for keeping me company in our student room.

A big thanks goes to SRON, to Wolfgang Wild and to the whole ALMA group, in which I was able to bring to completion the work presented in this thesis, and who gave me the fantastic opportunity to attend this year’s ISSTT conference in Pasadena. Thanks to the ALMA group, to the Kapteyn and to the G.U.F. for the financial support.

I would like to thank in particular all the people that I worked in close contact with during my final master project. Thanks to Andrey Baryshev and Ronald Hesper, who proposed this master project and helped me a lot with its realization during the last 8 months. Thank you Patricio for spending so many long days in the lab, for your help and for answering all my questions. I wish to thank all the technicians of the SRON workshop, and especially Klaas, for the way he taught me how to put a design into practice, for the nice discussions we had, and for the soups at lunchtime.

A big hug to the “Little Italy” community of Groningen: to Sara, Fabrizio and Giuseppe, to Filippo, Daniele, Alessio and Damiano; for all the moments spent together, the nights when we watched movies and ate the renowned cold cuts from Piacenza, for the fixed appointment on Saturdays on the Grote Markt to bite some fish and chips... I’ll miss you!

An affectionate thanks to all my family, my dad and mom, Matteo and Martina, for being always close to me and for backing all my choices. And a special thanks to Roberto for always being there, for his help, for his encouragement, and for making me happy.

Thank you all!

Michela

## RINGRAZIAMENTI

Due anni sono passati e ora sono alla fine del mio master...finalmente! Ci sono molte persone che hanno reso possibile ciò e che per questo voglio ringraziare.

Un grazie particolare al prof. Reynier Peletier che mi ha dato l'opportunità di frequentare questo nuovo master e che ha seguito il mio percorso durante questi due anni. E grazie naturalmente a tutte le persone del Kapteyn che ho conosciuto.

Grazie alla SRON, a Wolfgang Wild e a tutto il gruppo di ALMA dove ho potuto portare a termine il mio progetto finale di master e che mi hanno dato la possibilità di prendere parte al ISS'TT di quest'anno a Pasadena. Ringrazio il gruppo di ALMA, il Kapteyn e il GUF per il supporto finanziario.

Vorrei ringraziare le persone con cui ho lavorato più a stretto contatto durante la mia tesi. In particolare grazie ad Andrey Baryshev e Ronald Hesper per avermi proposto questo progetto e avermi aiutato a portarlo a termine in questi ultimi 8 mesi. Grazie anche a Patricio per aver passato lunghe giornate in laboratorio con me aiutandomi e rispondendo a ogni mia domanda. Grazie ai ragazzi del Workshop, e in particolare a Klaas, per tutti gli insegnamenti su come si realizza un oggetto partendo dal suo "disegno", per le belle chiacchierate e le zuppe a pranzo.

Un abbraccio a tutta la "comunità italiana" conosciuta durante questi due anni a Groningen. A Sara, Fabrizio e Giuseppe, a Filippo, Daniele, Alessio, Damiano: per tutti i momenti passati assieme, le serate a guardare film mangiando i famosi salumi piacentini, l'appuntamento del sabato al Grote Markt per gustare l'ormai leggendario "Fish and Chips"...mi mancherete!

Grazie a tutta la mia famiglia, a papà, mamma, Matteo e Martina, per essermi stati sempre vicino e per aver appoggiato ogni mia scelta.

E infine un grazie particolare a Roberto per esserci stato sempre, avermi aiutato, consolato durante i momenti "no" e soprattutto reso felice.

Grazie a tutti!

Michela